UNIVERSITY OF OKLAHOMA

GRADUATE COLLEGE

SYNOPTIC CHARACTERISTICS AND PRECURSORS TO SUBSEASONAL TO SEASONAL EXTREME PRECIPITATION EVENTS ACROSS THE UNITED STATES

A THESIS

SUBMITTED TO THE GRADUATE FACULTY

in partial fulfillment of the requirements for the

Degree of

MASTER OF SCIENCE IN METEOROLOGY

By

GREGORY JENNRICH
Norman, Oklahoma
2019

SYNOPTIC CHARACTERISTICS AND PRECURSORS TO SUBSEASONAL TO SEASONAL EXTREME PRECIPITATION EVENTS ACROSS THE UNITED STATES

A THESIS APPROVED FOR THE
SCHOOL OF METEOROLOGY

BY

Dr. Jason C. Furtado, Chair

Dr. Jeffrey B. Basara

Dr. Elinor R. Martin

Acknowledgments

This work could not be completed alone. The author would like to thank the thesis committee for their time, ideas, and assistance throughout the research process. I would like to thank Dr. Furtado for his assistance with the research, his mentorship, and his time spent editing. Furthermore, my family and friends deserve acknowledgement for their support throughout this process, especially Noah Brauer. The author thanks other members of the PRES^{2}iP research group, the Applied Climate Dynamics Group, and CHEWe research group for their contributions. This work is supported by the National Science Foundation under their Prediction of and Resilience against Extreme Events (PREEVENTS) program (Grant #1663840).

Table of Contents

List of Tables

List of Figures

Abstract

In the United States and throughout the world, extreme precipitation events are a major cause of loss in life, property, and economic progress. Although the science of hydrometeorology has made significant improvements to the prediction and understanding of these events in recent decades, there is still much to learn about these events in the subseasonal to seasonal (S2S) timescale. This thesis focuses on identifying synoptic patterns and possible precursors ahead of an extreme precipitation event over the contiguous United States (CONUS). First, we provide a robust definition for 14-day and 30-day "extreme precipitation events," based on running precipitation totals from Parameter Elevation Regression on Independent Slopes Model (PRISM) daily precipitation data. Criteria for the events include exceedance of percentile thresholds, spatial extent, and the distribution of rainfall over the event period. The CONUS is partitioned into different geographic regions in order to compare and contrast the synoptic patterns associated with events in different parts of the country. Using these identified events, atmospheric variables from reanalysis (e.g., geopotential height, zonal winds, and integrated vapor transport) are composited to understand the evolution of the atmospheric state before and during a sub-seasonal extreme precipitation event. Common synoptic signals seen during events include significant trough-ridge patterns, an energized subtropical jet stream, and enhanced integrated vapor transport into the area. Also, atmospheric river activity increases in the region during extreme events. Identified signals are similar for both 14-day and 30-day events, albeit with weaker composite anomalies for 30-day events. Further, the increases in frequency of atmospheric river activity is greater west of the Rockies, with respect to other regions, for 30-day events as compared to 14-day events. Modes of climate variability and lagged composites are investigated for their connection to 14-day extreme precipitation events and their potential use in lead time prediction. Key findings include synoptic anomalies in the North Pacific and regional connections

to modes such as the Pacific North American (PNA) pattern and the North Pacific Oscillation (NPO). Regional differences in these characteristics and possible reasons for them are discussed. Taken together, these results represent a step forward in helping forecasters to understand and identify sub-seasonal events in order to mitigate loss due to extreme precipitation events.

Chapter 1

Introduction

Extreme precipitation events are among the most devastating natural hazards in the contiguous United States (CONUS). These events pose significant risks and far-reaching impacts to life, property, and the economy. From 1980 to 2018, the top 30 United States (U.S.) inland flooding events cost a combined $124 billion USD and resulted in over 500 fatalities (National Centers for Environmental Information, 2019). Although flooding can arise from many sources (e.g., rapid snow pack melt, overflowing rivers/lakes, storm surge), heavy precipitation is a significant contributor. These losses emphasize the need for improved understanding and prediction of extreme precipitation events. The meteorology community, among others, particularly struggles with improving the predictability of extreme weather events (including hazards other than heavy precipitation like heatwaves, drought, and cold air outbreaks) on the subseasonal to seasonal (S2S) timescale (i.e., the period roughly spanning two weeks to three months) (Brunet et al., 2010; National Academies of Sciences, Engineering and Medicine, 2016). While daily or sub-daily extreme events have significant impacts, S2S extreme precipitation events tend to have more widespread losses due to the duration and the potential regional or larger scale of the events.

1.1 The S2S Timescale: Background and Previous Literature

With increasing interests by forecasters and users alike, the S2S timescale is an important period for which to increase the accuracy of weather forecasts and risk assessments. Yet, forecast skill and general insight into S2S forecasts is lacking compared to short term (1-10 day) and seasonal (3+ months) forecasts. The current capabilities of our short term numerical models do not extend skill into the S2S

timescale and most seasonal models do not consider S2S mechanisms or important modes operating on those shorter timescales. Thus, the S2S timeframe particularly lacks forecast skill, increasing its priority for research (Vitart and Robertson, 2018). Recently, several research projects have addressed this issue. For example, the S2S Prediction Project aims to improve forecast skill and fundamental understanding of the sources of S2S predictability, and promote its use by operational centers the application communities (Robertson et al., 2015; Vitart and Robertson, 2018). This project also includes a database to "help identify common successes and shortcomings in the model simulation and prediction of sources of subseasonal to seasonal predictability" (Vitart et al., 2017). Furthermore, this study is a part of the Prediction of Rainfall Extremes at Subseasonal to Seasonal Periods (PRES^{2}iP) project, funded through the National Science Foundation (NSF) Prediction of and Resilience against Extreme Events (PREEVENTS) program. A key goal of PRES^{2}iP is to enhance fundamental understanding of the large-scale dynamics and forcing of S2S extreme rainfall events. It is through projects such as these that the prediction and understanding of S2S events will improve.

While exploration into the S2S timeframe is a fairly recent endeavour, a wide array of meteorological/climate features have been investigated at the S2S time scale. For example, Batté et al. (2018) investigates the prediction of African heat waves in the S2S timeframe using two coupled forecasting systems, yielding mixed predictability results. Similarly, Schiraldi and Roundy (2017) explores the agricultural drought transition periods and their predictability in S2S models, finding more skill with 60-day agricultural droughts than 20-day agricultural droughts. Other features analyzed at the S2S time scale include: tropical rainfall in East Africa (Moron et al., 2013), Madden Julian Oscillation (MJO) prediction (Lim et al., 2018), and wintertime tornado variability across the CONUS (Molina et al., 2018). One topic that has been studied relatively less is S2S extreme precipitation events in the CONUS.

Yet, there are many occurrences of S2S extreme events accompanied with major socioeconomic impacts. The historic 1993 Mississippi River Basin flood is an example of such an S2S extreme precipitation event. This single event cost billions of dollars in damage and was forced, in part, by persistent atmospheric patterns favoring frequent heavy precipitation episodes across the central US (e.g., Kunkel et al., 1994). Additionally, the June/July 2006 Mid-Atlantic extreme precipitation event was also high impact, with widespread losses in life and property due to severe flooding resulting from the rainfall. A combination of anomalous transport of moist tropical air and a blocking ridge lead to this extended period of rainfall (e.g., Gitro et al., 2014). More recently, a series of shortwave troughs and anomalous moisture resulting in heavy rainfall over Oklahoma and Texas during May and June 2015 lead to widespread flooding and extensive damage (e.g., Wang et al., 2015). Records for monthly precipitation totals were shattered across Oklahoma and parts of Texas, including for Oklahoma City (19.48 inches) and the Oklahoma statewide average (14.40 inches) (Oklahoma Mesonet, 2015). A more complete understanding of these events may help forecasters predict them and public officials prepare for the multiple impacts of these prolonged heavy rainfall episodes.

1.2 Previous Literature on Extreme Precipitation

Past studies on extreme precipitation events have examined long-term precipitation trends, specific case studies of extreme events, and characteristics of *daily* extremes, often in a specific region. Several studies (e.g., Karl and Knight, 1998; Mallakpour and Villarini, 2016; Armal et al., 2018) have indicated that the frequency of extreme precipitation and annual totals have increased across several regions of the U.S. over the last half century, particularly in areas east of the Rocky Mountains. Armal et al. (2018) find that 59.6% of the stations sampled featured no long term ($\sim$100 years) trend in precipitation. For the stations with trends, well over half could

be attributed to anthropogenic forcing. An increase in CONUS precipitation may be in-part attributed to increases in $\geq 90^{\text{th}}$ percentile precipitation events (Karl and Knight, 1998). In terms of extreme precipitation, Mallakpour and Villarini (2016) suggested the frequency, but not magnitude, of heavy precipitation is increasing over large areas of the CONUS, with the exception of the Northwestern U.S. and northern California. In regional studies, Frei et al. (2015) found significant increases to summertime precipitation in the Northeast U.S. Similarly, rainfall variability and intensity has been increasing in the Southeast U.S. during boreal summer months (Wang et al., 2010; Weaver et al., 2016).

Case studies of impactful precipitation events have focused on improving predictability or understanding of particular features. Marciano and Lackmann (2017) explored the contribution of Hurricane Joaquin to excessive rainfall and resultant flooding in South Carolina during October 2015 and concluded the hurricane slowed the progression of the upper level trough and provided diabatic enhancement of the jet streak in the Southeast U.S. This set the stage for excessive moisture flow into the region and a multi-day heavy rainfall event. Similarly, Tennessee and Kentucky endured a costly three-day extreme rainfall event during May 2010. Lynch and Schumacher (2014) analyzed the European Centre for Medium-Range Weather Forecasts (ECMWF) medium-range Ensemble Prediction System and found that ensemble members with weaker low pressures and a more elongated trough predicted the event the best. Under future climate change, a May 2010-like event may worsen in terms of total precipitation due to the increased water vapor content and stronger convective updrafts (e.g. Lackmann, 2013; U.S. Global Change Research Program, 2018). Although these referenced events are not S2S events per se, these analyses identify processes and features that could play an important role in S2S extreme precipitation events.

Key characteristics of daily to sub-weekly extreme precipitation have been identified over several spatial domains: the CONUS as a whole (e.g., Zhao et al., 2017; Touma et al., 2018), and various subregions of the CONUS (e.g., Konrad, 2001; Schumacher and Johnson, 2006; Moore et al., 2015; Collow et al., 2016; Chiodi et al., 2016). These works noted particular patterns of precipitation characteristics (seasonality, spacial scale, etc.), anomalous geopotential heights, and/or enhanced moisture transport that result in extreme precipitation events. Zhao et al. (2017) identified 'extreme precipitation patterns' via hierarchical cluster analysis of daily precipitation anomalies. These patterns vary spatially with season and model type. Similarly, using a CONUS station network and indicator semivariograms, length scales of daily precipitation events are found to vary both regionally and seasonally (Touma et al., 2018). 2-day extreme precipitation events of differing spacial scales east of the Rockies are analyzed in Konrad (2001), noting some of the geographical, seasonal, and synoptic characteristics of these events. Furthermore, Schumacher and Johnson (2006) examined the weather systems (among other attributes) associated with 24-hour extreme precipitation events. While MCS events are the leading contributor in most regions, synoptic and tropical systems are found to be important drivers for extreme precipitation in the South, Southeast, and Northeast U.S.

In terms of research into specific characteristics of regional extreme precipitation events, there are several examples:

- Non-tropical 24-hour extreme precipitation events in the Southeast U.S. are driven by a combination of dynamical (maximized in the cold-season) and thermodynamic (maximized in the warm-season) influences leading to precipitation amounts and duration for events generally maximized in the spring and autumn (Moore et al., 2015).

- Daily summertime extreme precipitation events in the Northeast U.S. are characterized by significantly anomalous vertically integrated moisture flux, precipitable water, 200 hPa winds, 500 hPa heights, and sea level pressure (Collow et al., 2016).

- In Chiodi et al. (2016), summertime rainfall events in Eastern Washington and Oregon are characterized by 500 hPa flow directions. Southwest 500 hPa flow is the most frequent and more favorable for precipitation days near the Pacific Coast than the interior Pacific Northwest. Southeast 500 hPa flow is more favorable for precipitation for the interior Pacific Northwest and has greater tendency for lightning activity.

These are just some examples of studies on extreme precipitation on or near the daily time scale. With similar analysis, but working in a different timeframe, Flanagan et al. (2018) examines characteristic atmospheric patterns associated with extremely rainy (i.e., pluvial) years in the U.S. Great Plains. The study found that the characteristic atmospheric patterns during pluvial years are driven by synoptic scale processes rather than low-frequency features and also differ between the Northern and the Southern Great Plains.

A recurring theme in many of these studies is that moisture and mechanisms for its transport play a major role in these events. As such, atmospheric rivers (ARs) were suggested as an important medium for moisture transport (e.g., Newell et al., 1992), and thus identifying ARs has been a useful way of investigating moisture transport associated with extreme precipitation events (Wick et al., 2013; Guan and Waliser, 2015). ARs are a key aspect of extreme precipitation events throughout many regions in the U.S. including, the Central U.S. (Lavers and Villarini, 2013), the Intermountain West (Rutz et al., 2015), the Southeast (Mahoney et al., 2016), and the West Coast (e.g., Neiman et al., 2011; Dong et al., 2018; Dettinger et al.,

2018). Yet, we lack a complete understanding of the role ARs play specifically for S2S precipitation extremes.

Finally, the role of large-scale modes of climate variability in S2S extreme precipitation events remains to be quantified. Individual events, like the anomalously cold North American winter of 2013/14, have been connected to extreme and persistent high-amplitude climate modes like North Pacific Oscillation (NPO) and West Pacific teleconnection pattern (Baxter and Nigam, 2015). The NPO index represents anomalies of the meridional dipole of sea level pressure in the North Pacific Ocean, which is closely related to anomalous geopotential heights captured by the West Pacific teleconnection. The El Niño Southern Oscillation (ENSO) phenomenon, a measure of anomalous sea surface temperatures in the equatorial Pacific Ocean, has been assessed as a tool for the predictability of CONUS wintertime daily extreme precipitation and has shown some skill, particularly in the Great Plains (Gershunov, 1998). Perhaps the most recognized teleconnection related to precipitation prediction is the MJO. The MJO is represented physically by an area of deep convection that circumnavigates the globe every 30 to 90 days and can help to bridge the gap between weather and climate (Zhang, 2013). The connection between extreme precipitation and the MJO has been explored globally (Jones et al., 2004) and especially in Western U.S (e.g., Guan et al., 2012; Mundhenk et al., 2018). However, there has not been in-depth analysis into whether or not precursory features exist in mode indexes for a collection of S2S events.

1.3 Thesis Goals and Hypotheses

Given the increased emphasis on the predictability in the S2S framework and the impactful nature of extreme precipitation, this thesis addresses some of the gaps in understanding in sub-seasonal extreme precipitation events. More specifically, 14-day

and 30-day extreme precipitation events are analyzed for their fundamental characteristics in precipitation (seasonality, event variability, and accumulation distribution) and synoptic features. Additionally, connections to large-scale modes of climate variability are examined for the 14-day events. These extreme events are established in a regional framework, allowing for comparisons between regions within the CONUS and a better understanding of the evolution of sub-seasonal extreme precipitation in those regions. We hypothesize that both 14-day and 30-day extreme precipitation events identified have similar synoptic features (i.e., anomalous troughing, jet streaks, and enhanced moisture transport) to daily events, and climate indices for 14-day events support favorable synoptic anomalies for above average precipitation, as past studies have indicated. Yet, we expect an increase in the duration of these anomalous features and indices when compared to previous work, placing them in the S2S timeframe. Furthermore, we hypothesize a close relationship between the anomalous patterns of 14-day events and 30-day events, albeit with the possibility of reduced magnitudes in composite anomalies for the longer term events.

The thesis is organized as follows. Data and methodology used for this study, including the event identification algorithm, are described in chapter 2. Chapter 3 contains the results of the composite analysis for synoptic features associated with both 14-day and 30-day events, including anomalous troughing and ridging and AR activity. Lag composites of several atmospheric variables and modes of climate variability for the 14-day extreme precipitation events are discussed in chapter 4. A summary and discussion of results is provided in chapter 5.

Chapter 2

Data and Methods

2.1 Data

All precipitation data are from Parameter Elevation Regression on Independent Slopes Model (PRISM), which provides daily precipitation from 1981 to present with a 4 km resolution (Daly et al., 2000; PRISM Climate Group, 2017). These temporal and spatial scales are sufficient to analyze S2S extreme precipitation events and their synoptic characteristics. Atmospheric variables from the ECMWF Re-analysis Interim (ERA-Interim) daily data with a 2.5° x 2.5° longitude/latitude resolution (Dee et al., 2011) are used to investigate the synoptic features associated with, and preceding, S2S extreme precipitation events. Variables include geopotential heights, zonal winds, and specific humidity. The latter two variables are used to quantify intergrated vapor transport (IVT), a measure of vertically intergrated column of moisture, calculated following the methodology of Dettinger et al. (2018) and others:

$$IVT = -\frac{1}{g}\int_{1000hPa}^{200hPa}(q * \vec{V}_h)dp \tag{2.1}$$

where $\vec{V}_h$ is the horizontal wind, q is specific humidity, and g is the acceleration due to gravity.

As mentioned in Chapter 1, ARs are a common driver of extreme precipitation and single day heavy rainfall. Here, we apply our own AR framework to S2S extreme precipitation events. In order to achieve this, we use a database of ARs based on a detection algorithm developed by Guan and Waliser (2015). This 6-hourly algorithm includes three key requirements for ARs. First, IVT must be greater than the 85th percentile and greater than 100 kg m^{-1} s^{-1}. Next, the mean AR IVT direction must

be within 45° of the orientation of the AR shape and have an 'appreciable' poleward component. Finally, the length of the AR must be greater than 2000 km and have a length-to-width ratio greater than 2. Every identified AR is given an axis, which is defined as the points along the center of the AR, and a shape, which is the extent of the AR.

In addition to synoptic variables, modes of climate variability are also explored to identify possible connections to and predictability of S2S extreme precipitation events. The daily indexes for the Arctic Oscillation (AO) (Thompson and Wallace, 2000), NPO (Rogers, 1981), North Atlantic Oscillation (NAO) (Wallace and Gutzler, 1981), and Pacific North American (PNA) (Wallace and Gutzler, 1981) are provided by the NOAA Climate Prediction Center (CPC) (`https://www.cpc.ncep.noaa.gov/products/precip/CWlink/`). Additionally, we consider the MJO, with the phase and amplitude, via the Wheeler and Hendon (2004) index, of the MJO provided by the CPC. These indices were chosen based on previous studies linking climate modes to extreme precipitation events (e.g. Kenyon and Hegerl, 2010; Jones and Carvalho, 2012; Jiang et al., 2014; Baxter and Nigam, 2015; Mundhenk et al., 2018).

2.2 Defining 14-Day and 30-Day Extreme Precipitation Events

To examine extreme precipitation events across the CONUS, we developed a robust algorithm to identify these events. First, we compute the distribution of 14-day (30-day) precipitation cumulative totals for each point using a running 14-day (30-day) moving window from 14 (30) January 1981 to 31 December 2010. We choose the 95^{th} percentile of the distribution as the threshold to define extreme precipitation at each location. The use of the 95^{th} percentile is a common threshold in studies investigating extreme precipitation and allows us to investigate impactful events (Alexander et al., 2006; Frei et al., 2015; Collow et al., 2016). Note that similar works also use

days with a minimum precipitation threshold (e.g., Rivera et al., 2014; Collow et al., 2016; Hirata and Grimm, 2017). When considering S2S events, this consideration need not apply due to the longer temporal scale being analyzed.

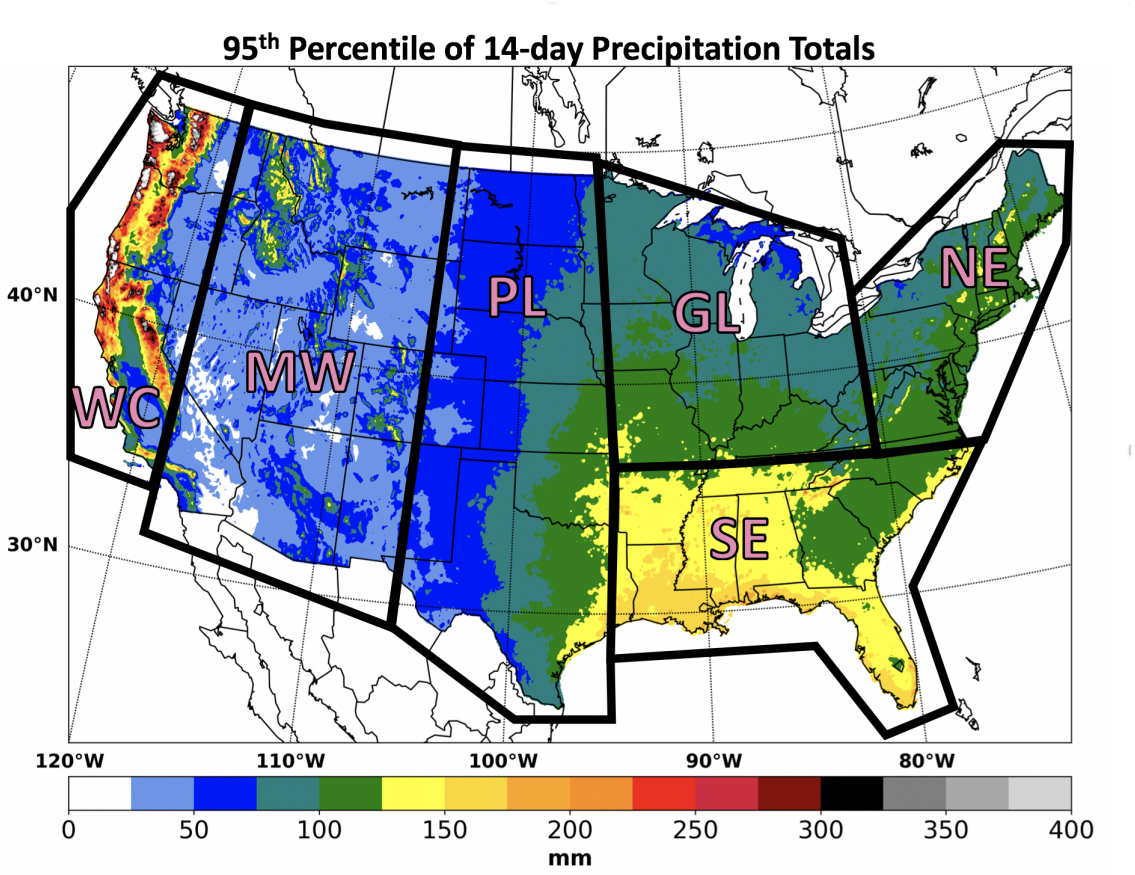

Figure 2.1: The 95th percentile of the distribution for 14-day precipitation totals from 1981-2010. The six regions of study for the CONUS are delineated by black polygons.

Fig. 2.1 illustrates a map of the 95th percentile values of 14-day precipitation totals. We further divide the CONUS into six geographic regions in order to compare and contrast characteristic patterns associated with S2S extreme precipitation events in different parts of the country. The six different regions in this study are the Northeast (NE), Southeast (SE), Great Lakes (GL), Great Plains (PL), Mountain West (MW), and West Coast (WC). The regions are chosen based on similarities in values of the 95th percentiles themselves, climate classifications given in Kottek et al. (2006),

and geo-political boundaries. Our regional breakdown is similar to other extreme precipitation studies (e.g., Slater et al., 2016; Saharia et al., 2017). While there are many methods of partitioning the CONUS into regions, the delineation chosen for this study allows for a set of largely recognized regions, which are sizable enough to identify regional S2S extreme precipitation events.

Table 2.1: 14-day extreme precipitation event criteria differences between regions and the number of events analyzed in each region.

95^{th} Percentile 14-Day Events						
	NE	**SE**	**GL**	**PL**	**MW**	**WC**
Area Criteria $(Km)^2$	$\geq$ 200,000	$\geq$ 300,000	$\geq$ 300,000	$\geq$ 300,000	$\geq$ 200,000	$\geq$ 200,000
# of Precipitation days	5	5	5	5	3	5
14-Day Event Count	28	36	36	41	39	39

Working within a regional framework, 14-day extreme precipitation events are identified with the following criteria and considerations (Table 2.1). First, the total area, based on the number of grid-boxes meeting or exceeding their 95^{th} percentile threshold, is calculated for every 14-day moving window. If the total area exceeds $200\,000\,\text{km}^2$ or $300\,000\,\text{km}^2$ (see Table 2.1), it is considered a possible event. We then set two exclusionary criteria for events. First, if the number of days of area-averaged precipitation exceeding $10\,\text{mm}\,\text{d}^{-1}$ is less than 5 days (3 days in the MW), we exclude that event. This criterion ensures multiple days of precipitation during the period. Second, if the precipitation total for the day of the heaviest precipitation along with the day before and day after make up greater than 50% of the cumulative total precipitation for that 14-day period, the event is disregarded so as to avoid a smaller temporal scale event from being the leading driver of a S2S event. Finally, if any 14-day periods are overlapping with another event window, the 14-day window with the greatest cumulative precipitation is chosen, as not to have any events overlapping. Altogether, this approach ensures a comparable number of events in each region.

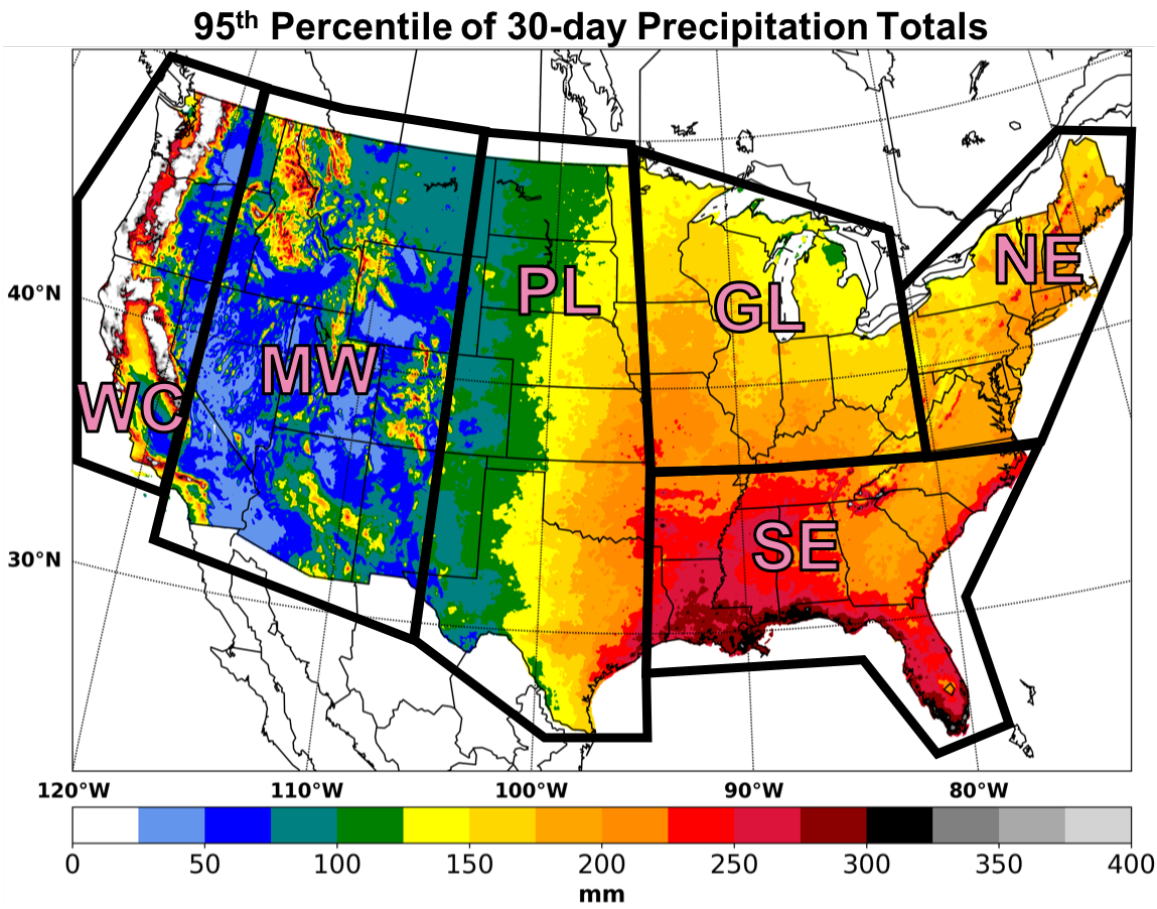

Figure 2.2: Same as in Fig. 2.1, but for 30-day precipitation totals.

Table 2.2: 30-day extreme precipitation event criteria differences between regions and the number of events analyzed in each region.

95^{th} Percentile 30-Day Events						
	NE	**SE**	**GL**	**PL**	**MW**	**WC**
Area Criteria $(Km)^2$	$\geq$ 200,000	$\geq$ 300,000	$\geq$ 300,000	$\geq$ 300,000	$\geq$ 200,000	$\geq$ 200,000
# of Precipitation days	8	8	8	8	5	8
30-Day Event Count	22	23	20	17	17	25

Fig. 2.2 displays the 95^{th} percentile values for 30-day precipitation totals in the same regional framework as Fig. 2.1. 30-day extreme precipitation events are identified with the same algorithm as 14-day events, but with a few changes to the criteria. It should be noted that the identification of 14 and 30-day events is performed independently to one another, thus some 14-day extreme precipitation events occur during

30-day extreme precipitation events. Approximately 60% of 30-day events have some overlapping with 14-day events. Table 2.2 documents the criteria for 30-day events in each region, along with the total event counts. The area threshold is left unchanged at 200 000 km^2 or 300 000 km^2 in a region. The number of precipitation days (i.e. the number of days of area-averaged precipitation exceeding 10 $mm\,d^{-1}$) increases to eight (5 in the MW region). While the logical increase would see this threshold at ten, accounting for the doubling of days in the event window, the number of events meeting the threshold is not enough to allow for proper analysis. Thus, many events did not have ten or more precipitation days. The second exclusionary criteria is also the same as in the 14-day algorithm, though likelihood of a smaller temporal scale event from being the leading contributor to a 30-day event is small. Finally, the same overlapping/neighboring considerations in place for 14-day events are used for determining the exact window examined in 30-day events.

2.3 Compositing Methods

With a list of 14-day and 30-day extreme precipitation events for each region, composites of the ERA-Interim variables are then used to identify significantly anomalous patterns for each region. For 14-day events, three distinct time periods are chosen for compositing: (1) the 14 days during events (i.e., Days +1 to +14); (2) Days -10 to -6 i.e., before the start of an extreme precipitation event; and (3) Days -5 to -1. Patterns identified during the event window help to characterize the regional aspect of 14-day extreme precipitation events. Patterns before the start of the event are explored for their utility in forecasting such events with different leads. For 30-day extreme precipitation events, the 30 days during events (i.e., Days +1 to +30) are composited and compared to the 14-day event composites. Statistical significance for all composites is based on a 5,000-iteration two-tailed bootstrapping test (with replacement).

Analysis of AR influences for 14-day and 30-day extreme precipitation events is performed using the axis and shape features of the AR from the Guan and Waliser (2015) dataset. Using these two attributes, AR days are identified in each region to signify AR activity in a region. For any of the 6-hourly time steps, if the AR axis is over land within a given region, and if the shape (i.e. the total area of the AR) is greater than $300\,000\,\mathrm{km}^2$ over land, then that day is considered an AR day. Our study examines the occurrence and significance of AR days during 14-day and 30-day extreme precipitation event days and non-extreme event days.

Chapter 3

Characteristics of S2S Extreme Precipitation Events

3.1 14-Day Extreme Precipitation Events

3.1.1 Event Statistics

We begin our analysis of 14-day extreme precipitation events with an examination of the events themselves and their fundamental statistics. The number of events in each region ranges from 28 in the NE region to 41 in the PL region (Table 2.1), or approximately 1 event per year. Fig. 3.1 presents a summary of distributions and statistics of the events per region. For the WC and MW regions, most 14-day extreme precipitation events occur during the extended boreal winter (November-February) (Fig. 3.1a, green and pink bars, respectively). The PL and GL regions exhibit a bi-modal seasonal distribution with a peak in frequency of events in June and again in early fall (Fig. 3.1a, gold and tan bars, respectively). 14-day extreme precipitation events in the NE and SE regions are more evenly distributed throughout the year (Fig. 3.1a, red and blue bars, respectively), with maxima during boreal spring and fall. These seasonality aspects of 14-day extreme precipitation events generally align with the expected seasons for the wettest seasons in each area, as expected given how the 95^{th} percentile is defined.

In terms of the yearly distribution of events (Fig. 3.1b), no long-term trends are apparent. Yet, some features stand out. First, the frequency of events is similar in all regions; i.e., a fairly variable distribution throughout the 30-year period. All regions have years with multiple events and years with none. Second, several years stand out as particularly anomalous. With a total of nine 14-day extreme precipitation events, 1993 is an above average year, specifically in the PL and GL regions. All PL

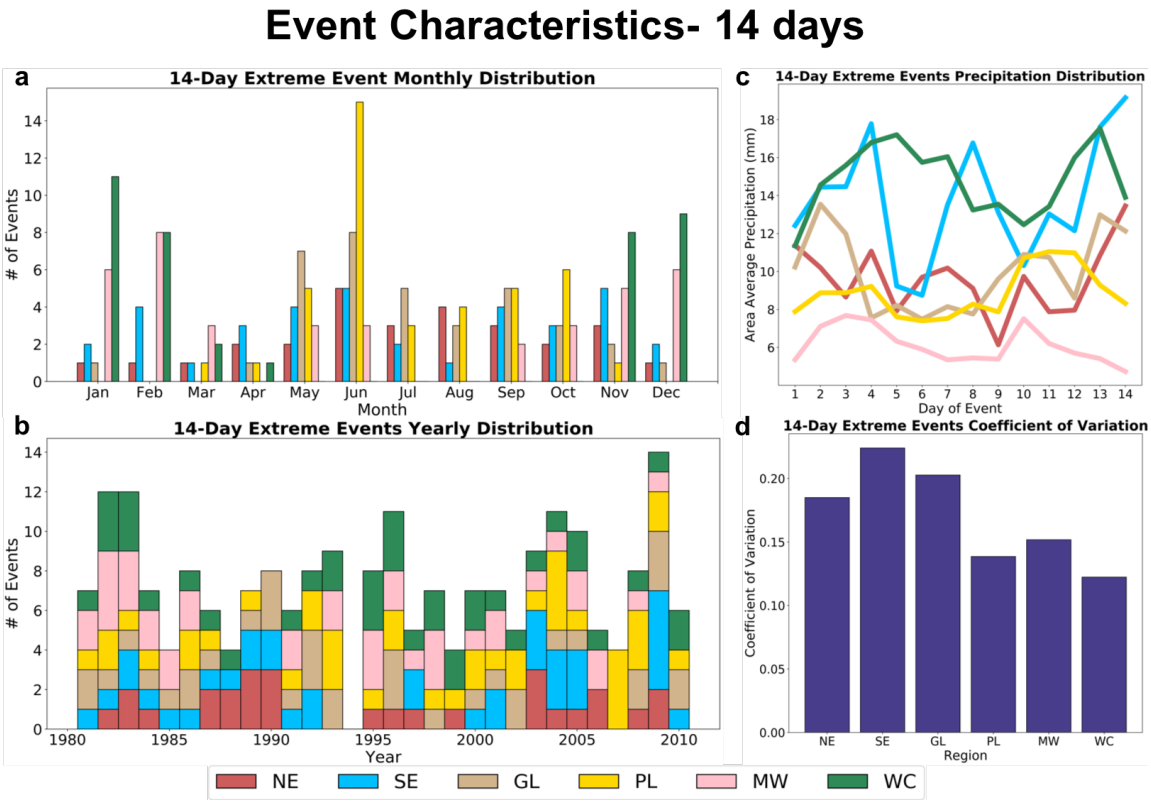

Figure 3.1: Various statistical comparisons of regional 14-day extreme precipitation events: (a) monthly event distribution, (b) yearly event distribution, (c) composite of the distribution of area average precipitation for each day of the event, (d) coefficient of variation (standard deviation of events/mean rainfall per day) in each region.

and GL events that year occurred between May and September (not shown), which correspond to the catastrophic Midwest flooding in the summer of 1993. Kunkel et al. (1994) identified specific multi-day heavy precipitation events which contributed to the flooding and find above average monthly precipitation in the Upper (Greater Upper) Mississippi Basin from April through August (April through September) 1993. While there were several other factors that lead to the flooding (i.e., heavy winter precipitation and snowpack; Kunkel et al., 1994), the events found in our study are likely significant contributors to the extreme precipitation that year. By contrast, zero 14-day extreme precipitation events occurred in 1994. Finally, 2007 was an overall very wet year in the PL region, where four events occurred. The exact contribution of

our identified events to yearly anomalies is outside the scope of this study, but 14-day extreme precipitation events could be an important contributor to pluvial years.

The differences in the distributions of precipitation during 14-day extreme precipitation events and the event-to-event coefficient of variation are displayed in Fig. 3.1c and Fig. 3.1d, respectively. A few observations are made from the distribution of event precipitation. First, the WC and SE regions have the greatest area-averaged precipitation (i.e., total area under the curve, Fig. 3.1c), while the MW region has the least. The three other regions have comparable totals to one another. This result corresponds well with the distribution of 95^{th} percentile of 14-day precipitation totals (Fig. 2.1), with the regions of greatest thresholds receiving the greatest total precipitation. Secondly, precipitation is overall evenly-distributed throughout 14-day extreme precipitation events in all regions, except for the SE region (Fig. 3.1c, blue line), suggesting that many events in the SE U.S. are made up of a few 'sub-events', during which 1-3 days of heavier precipitation occur. The SE region also has the greatest coefficient of variation (Fig. 3.1d). By contrast, the WC region has the smallest coefficient of variation, suggesting that WC events have relativity less event-to-event variability in area-averaged precipitation totals than any other region.

3.1.2 Synoptic Composites

To examine the state of the atmosphere during 14-day extreme precipitation events, we composite daily standardized anomalies of several variables over the entire 14-day period for all events. These variables are standardized by subtracting the daily mean from the reanalysis value and dividing the subsequent value by the long-term (1981-2010) standard deviation. Fig. 3.2 shows the average 500 hPa geopotential height standardized anomalies in each of the six regions. All geopotential height composites share a common theme: a trough-ridge pattern, with the trough (i.e., negative height anomalies) to the west of the specific region and ridging (i.e., positive

height anomalies) to the east. The WC region is the exception, with a meridional dipole in the Eastern Pacific (Fig. 3.2f). Furthermore, the relative magnitude of the trough-ridge pattern differs in each region. In the NE and WC regions (Fig. 3.2a and f, respectively), negative height anomalies are greater in magnitude than the corresponding positive height anomalies. The opposite is true in the GL region (Fig. 3.2c). These trough-ridge patterns are favorable for precipitation due to the positive differential vorticity advection and warm air advection promoting rising motion over the region (Bluestein, 1992). In a quasi-geostrophic framework, this resulting ascent downstream of the 500 hPa trough is supportive of the development of precipitation and has been tied to heavy rainfall (e.g., Maddox et al., 1979). Thus, a favorable synoptic geopotential height pattern is in place in all regions during 14-day extreme precipitation events.

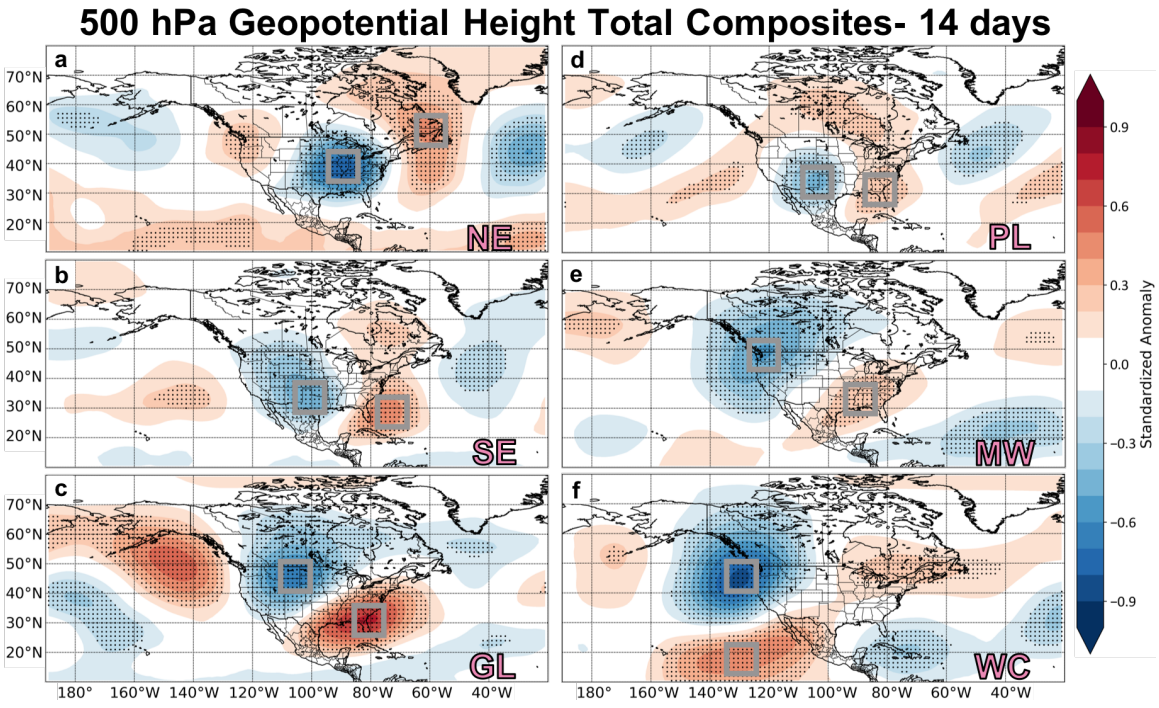

Figure 3.2: Composite of 500 hPa geopotential height standardized anomalies for 14-day extreme precipitation events in each region. Statistically significant ($p < 0.05$) anomalies are stippled. Gray boxes are 10° by 10° maxima areas for trough and ridge anomalies.

There is apparent nonuniformity in the exact orientation of the trough-ridge dipole, which is evident when examining the 200 hPa zonal wind standardized anomalies event composite (Fig. 3.3). The NE region composite (Fig. 3.3a) has an amplified zonal jet to the southwest of the region, putting the NE region in the left-exit region of a jet streak. The SE region (Fig. 3.3b) has the clearest jet streak feature with a maximum to the west and another to the northeast. This set-up resembles an ideal coupled jet pattern, with the SE region located in the left-exit region of one jet and the right-entrance region of another. A coupled jet pattern such as this favors upper level divergence creating synoptic scale lift (Bluestein, 1993). These upper level zonal wind and mid-level height patterns point to a favorable dynamical set up for synoptic scale precipitation. The GL and WC regions (Fig. 3.3c and f, respectively) have the most pronounced anomalies, suggesting enhanced zonal winds are important and occur over a large area in 14-day extreme precipitation events. All regions, except the PL region (discussed later), have significant zonal wind anomalies that are favorable for synoptically-forced precipitation.

Enhanced moisture transport into the various regions is also a main feature of 14-day extreme precipitation events. Figure 3.4 displays the total event composite of standardized anomalies of IVT. Vectors overlaid on positive (negative) anomalies signify increased (decreased) total column vapor transport in the direction of the vector. In all regions, large cyclonic and/or anti-cyclonic features set-up in patterns favorable for enhanced moisture transport. The NE, MW, and WC regions (Fig. 3.4a,e,f) are dominated by cyclonic features co-located with troughing in those areas, suggesting that the moisture transport is likely driven by the synoptic scale pattern. The SE, GL, and PL regions (Fig. 3.4b,c,d) have large southerly anomalies with a clear moisture source in the Gulf of Mexico. There is also anomalous westerly flow in the east Pacific for the SE and PL regions, suggesting possible Pacific moisture influences in these regions. The WC region has some of the most anomalous IVT,

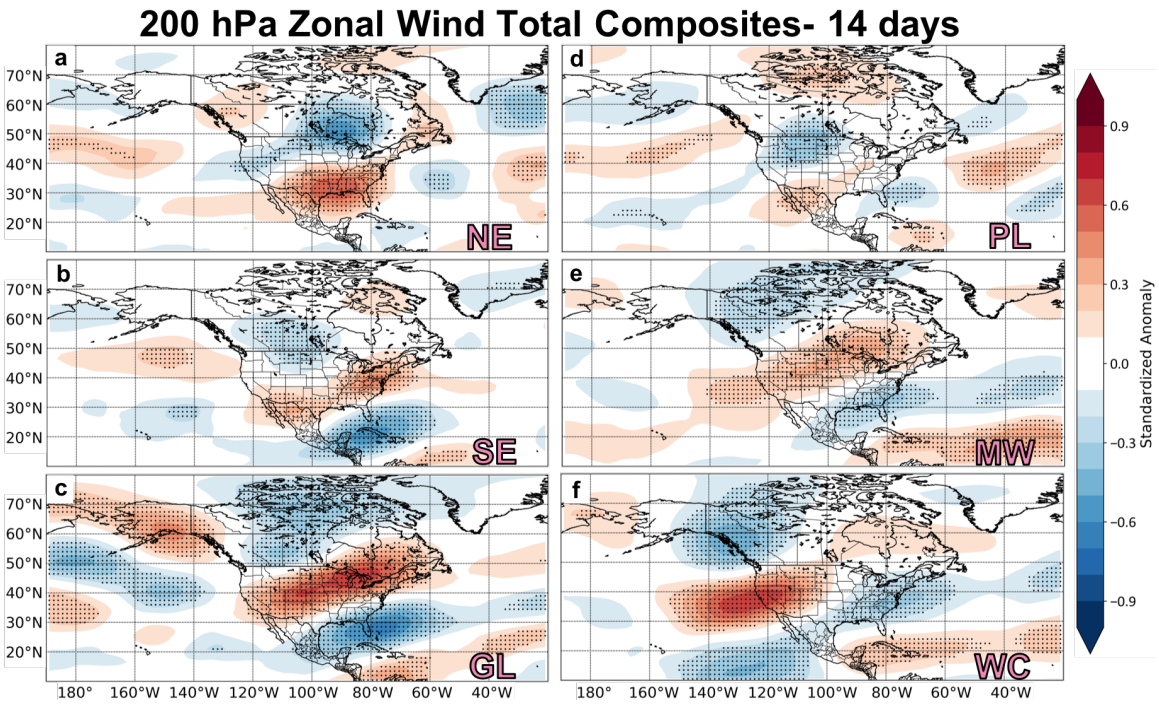

Figure 3.3: As in Fig. 3.2, but for 200 hPa zonal winds.

implying flow from the central and eastern Pacific is fundamental for these events. In general, IVT anomalies indicate increased moisture transport into a region occurs during 14-day extreme precipitation events.

One aspect of moisture transport missing in the column IVT analysis performed in Fig. 3.4 is the differentiation between low- and upper-level moisture transport. To address the differences between the lower tropospheric moisture transport and upper tropospheric moisture transport, the IVT analysis in Fig. 3.4 is divided into lower level IVT (1000-700 hPa) and upper level IVT (700-200 hPa) and upper level IVT is subtracted from the lower level IVT (Figure 3.5). As Fig. 3.5 indicates, each region has areas of upper tropospheric dominant moisture transport (blue contours) and lower tropospheric dominant moisture transport (red contours). The NE region (Fig. 3.5a) has the least difference between the two levels, suggesting upper and lower IVT anomalies are of equal importance for S2S extreme precipitation events in that region. The regions with the Gulf of Mexico as a moisture source (i.e. SE, GL, PL, and MW)

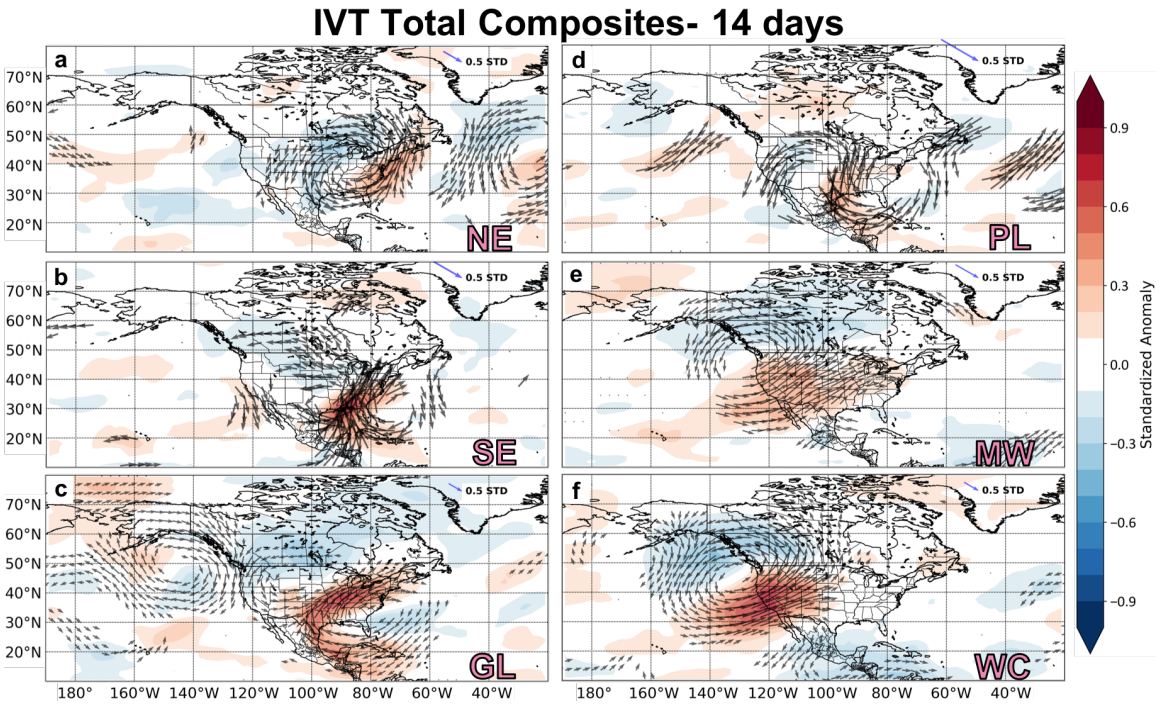

Figure 3.4: Composite of standardized anomalies of IVT magnitude for 14-day extreme precipitation events in each region is contoured. Vectors depict the standardized anomalies of the u and v components of IVT. Only significant ($p < 0.05$) vector anomalies are plotted.

have lower level dominant IVT from the Gulf into the specific region. The GL region (Fig. 3.5c) has the most pronounced influence of both levels. Low level IVT is focused over the Gulf and the Southern US, while upper level IVT is more predominant across the Central and North Central U.S, where the zonal wind anomalies are the strongest (Fig. 3.3c). These coinciding features suggest the increased upper level zonal winds greatly contribute to the IVT anomalies via eq. 2.1. The WC region in Fig. 3.5f has a similar contribution to upper level IVT from enhanced upper level zonal winds in Fig. 3.3f. Both upper and lower level IVT anomalies represent key features to 14-day extreme precipitation events.

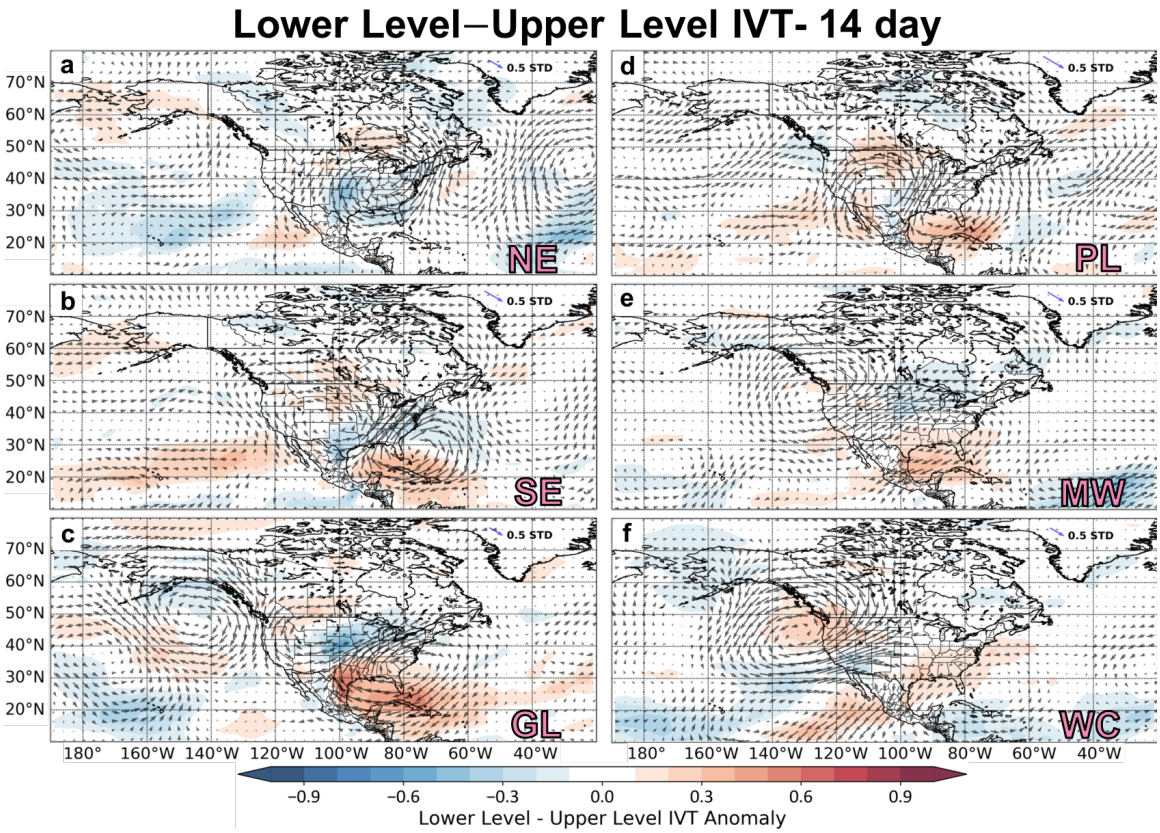

Figure 3.5: Composite of standardized anomalies of the difference between lower level (1000-700 hPa) and upper level (700-200 hPa) IVT magnitude for extreme event days in each region is contoured. Red (blue) contours represent greater lower level (upper level) IVT influence to total IVT standardized anomalies. Vectors depict the standardized anomalies of the u and v components of column total IVT.

3.1.3 Trough-Ridge Patterns

The total event composites illustrate the importance of synoptic patterns for 14-day extreme precipitation events, particularly the prominent ridge-trough dipole pattern seen in all regions. To examine this prominent feature more closely, we construct time series for the standardized height anomalies in the trough and ridge maxima regions (the 10° by 10° boxes depicted in each panel of Fig. 3.2). Fig. 3.6a-d shows the resulting time series for the NE and WC regions. While other regions have similar time series and evolution, these regions are chosen to contrast the signals leading up to and during 14-day extreme precipitation events. Every day during the events in the

NE region (Fig. 3.6a), the composite trough index indicates statistically significant ($p < 0.05$) negative anomalies. Over the same period, the standardized geopotential height anomalies in the NE ridge index are positive but not always significant, suggesting the troughing feature dominates this region. In the days leading up to the start of 14-day extreme precipitation events, the trough signal appears up to 4 days before, but the ridge signal is absent until the event starts. The lack of ridging before the start of events suggests ridging is not a precursor to NE events.

The WC region trough and ridge time series (Fig. 3.6c and d) are similar to those for the NE region during the events, but the WC region time series have greater magnitudes for the anomalies and a significant ridge signal during every day of the event. While the NE region has no signal beyond 4 days before the start of an event, the WC indices indicate strong ridging (troughing) 4 to 6 days (6 to 8 days) before events start occurs over the WC region trough (ridge) area. This reversal in geopotential height anomalies is unique to the WC and can be used as a possible precursor feature of WC 14-day extreme precipitation events.

With a better understanding of the evolution of the trough-ridge pattern in each region, Figs. 3.6e and f quantify the frequency of such anomalies relative to climatology via percentage of occurrence of trough and ridge days for event and non-event days. Non-event days represent all other days in the 30 year period that are not identified as event days. Days in which the standardized anomaly is less than (greater than) 1σ for the trough (ridge) box are called Trough (Ridge) days. A third separate classification quantifies days that meet both Trough-only day and Ridge-only day criteria: i.e., Trough/Ridge days. For the NE, Trough-only days are significantly more frequent during 14-day extreme precipitation events with Trough-only days occurring in over 25% of event days, while Ridge-only days occur in nearly 13% of event days. Trough/Ridge days are also more frequent, with occurrence around 14% of event days compared to just 3% in all other days. The WC region has more Trough/Ridge days

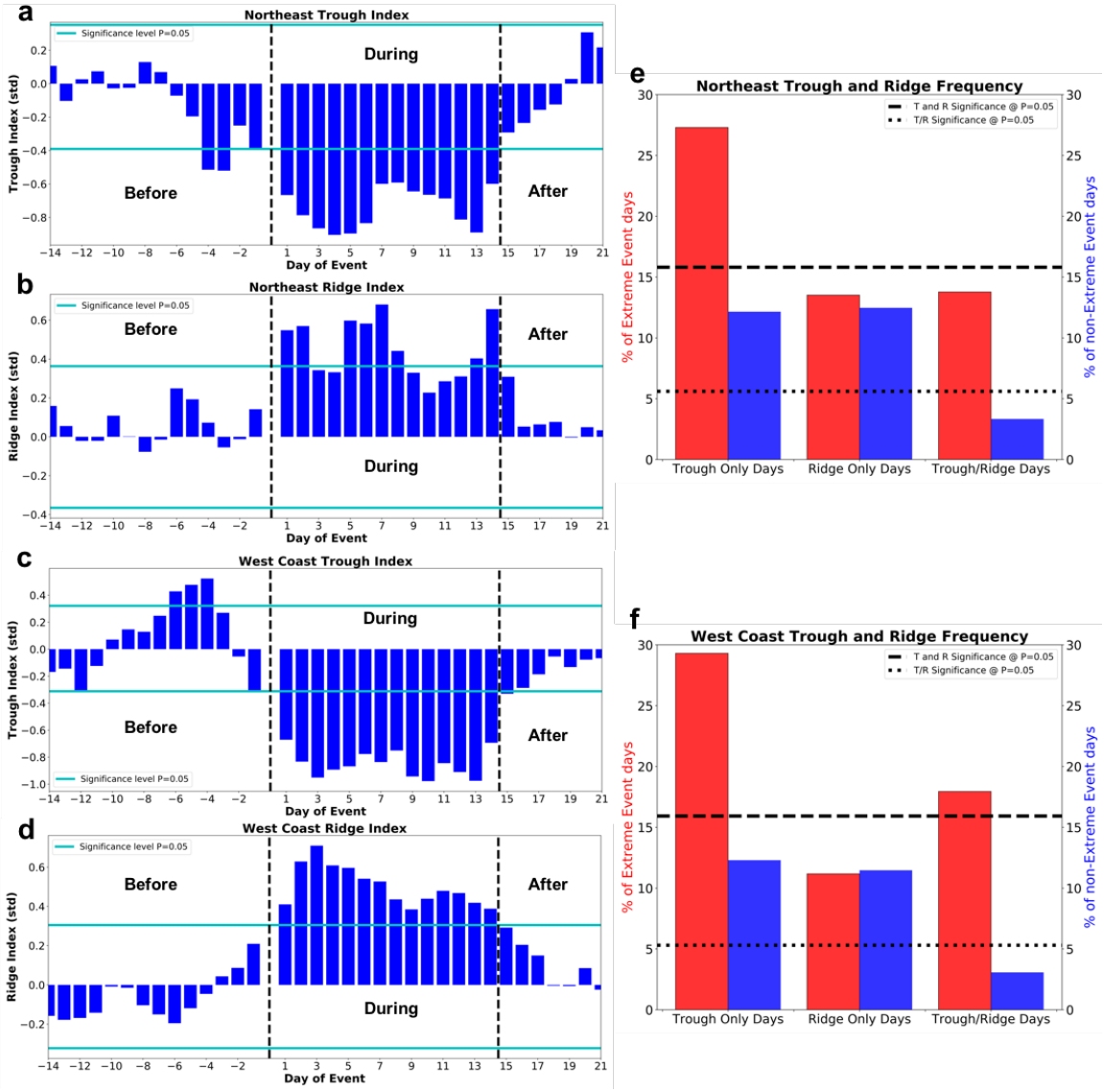

Figure 3.6: Eulerian trough and ridge statistics based on the area average of geopotential heights anomalies in the gray boxes in Fig. 3.2. Timeseries of composites for the standardized anomalies for the trough and ridge areas are plotted before, during, and after events for the (a) NE and (c) WC. The percentages of occurrence of Trough Only Days, Ridge Only Days, and Trough/Ridge Days for during extreme event days (red) and non-extreme event days (blue) for the (b) NE and (d) WC. Level for a statistically significant ($p < 0.05$) increase in percentage of occurrence is dashed (dotted) for Trough Only and Ridge Only days (Trough/Ridge Days).

than the NE region, likely resulting in a reduction of Trough-only and Ridge-only days. Adding the Trough/Ridge days and the Trough-only days together, the WC region has anomalous troughing in the designated region on over 45% of 14-day extreme precipitation event days. Furthermore, in both the WC and NE regions, Trough-only days are more frequent and troughing indices are more anomalous than their ridge counterparts (Figs. 3.6a-d), indicating that mid-level troughing plays a more important role than ridging in these regions. In fact, the preeminent role of troughing is found in all regions, except for the GL region where the southeast ridge seems to be a bigger influence to 14-day extreme precipitation events (not shown).

3.1.4 Atmospheric Rivers

We next explore how ARs contribute to 14-day extreme precipitation events in the CONUS. Fig. 3.4 illustrates that anomalous IVT into a region is a prevailing characteristic of 14-day extreme precipitation events, which has a close connection to ARs (Newell et al., 1992). AR days, a proxy for landfalling AR activity, are calculated in each region using the Guan and Waliser (2015) AR database. Fig. 3.7a compares the frequency of AR activity during event and non-event days, again where non-event days are all other days in the 30 year period that are not identified as event days. All regions have an increase in AR days during extreme event days than non-extreme days. The NE, SE, and WC regions have the smallest percentages of AR days for non-event days, but Guan and Waliser (2015) find these areas of the U.S. have higher AR frequency than the GL, PL, and WC regions. Thus, we need to compare the differences between the event AR days and the non-event AR days to get a better sense of the changes in AR frequency. The WC, GL, and SE regions have the greatest of the differences, suggesting that AR frequency increases the most in these areas.

Next, we examine the significant number of AR days during our 14-day extreme precipitation events, which serves as the baseline value. Any number of AR days

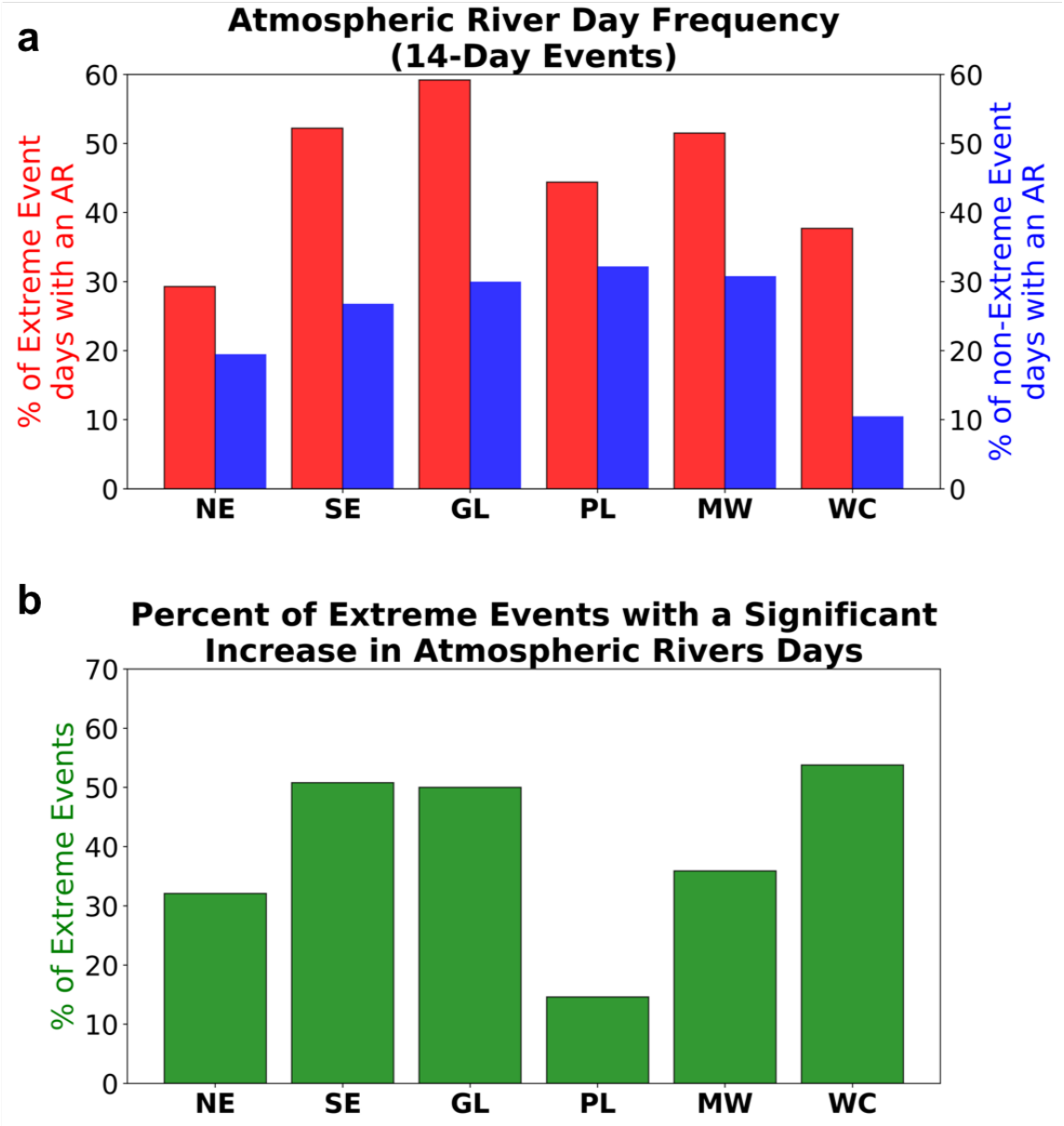

Figure 3.7: (a) The percentage of occurrence of AR days during extreme events (red) and non-extreme events days (blue) in each region. (b) The percentage of 14-day extreme precipitation events with a statistically significant ($p < 0.05$) number of AR days in each region.

beyond the baseline represents an anomalous increase in ARs in a 14-day period. Fig. 3.7b shows the percentage of our 14-day extreme precipitation events that meet or exceed this baseline. For example, it can be said that 50% or 18 of the 36 GL events have a significant number of AR days. The analysis indicates that AR frequency tends to increase during 14-day extreme precipitation events. The greatest increase in AR frequency occurs in the SE, GL, and WC regions. With $\geq$50% of events corresponding to a significant increase in AR activity, ARs are a particularly important characteristic of 14-day extreme precipitation events in these three regions. This result is in agreement with Figs. 3.4c and f, where the SE, GL, and WC regions have the most anomalous IVT into their respective region.

3.2 30-Day Extreme Precipitation Events

3.2.1 Event Statistics

In order to address a longer window of extreme precipitation and move further into the S2S timeframe, we next examine the characteristics of 30-day extreme precipitation events. We again begin with fundamental statistics of the events themselves. Table 2.2 displays the event identification algorithm criteria and the number of events in each region. For 30-day extreme precipitation events, the total counts range from 17 to 25 events. Given the number of days in each event is more than double, the number of events was expected to decrease. Note, that 14 and 30-day events are identified separately, thus there is over lapping dates. Near 60% of 30-day events overlap with 14-day events. The monthly distribution of the 30-day extreme precipitation events (Fig. 3.8a) has many similarities to the 14-day event monthly distribution (Fig. 3.1a), noting the month of the event is based on the midpoint day for each event. The PL and GL regions again have a bi-modal distribution with a main peak in the late-spring/early-summer and a secondary peak in the early fall (Fig. 3.8a, gold and tan bars, respectively). The NE region also has a bi-modal distribution,

which is in contrast to the more even distribution seen in Fig. 3.1a. The majority of the MW and WC 30-day extreme precipitation events occur between November and February (Fig. 3.8a, green and pink bars, respectively). The SE region (Fig. 3.8a, blue bar) again has a relatively even distribution. Generally, these 30-day extreme precipitation events occur in climatologically wet months for each respective region.

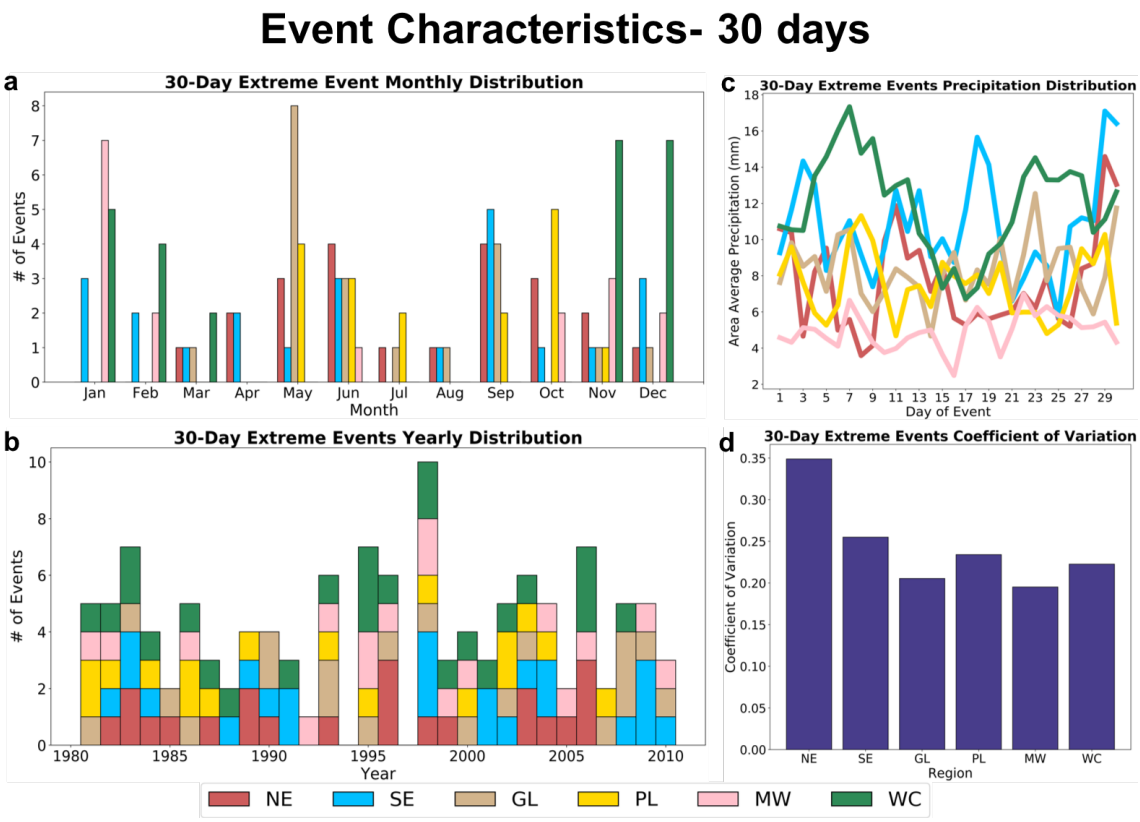

Figure 3.8: As in Fig. 3.1, but for 30-day extreme precipitation events.

As for the yearly distribution of 30-day extreme precipitation events (Fig. 3.8b), three to four events occur per year on average, with a fair amount of year-to-year variability. There are no events in 1994, but ten 30-day extreme precipitation events in 1995 (Fig. 3.8b). During the catastrophic Midwest flooding of the summer of 1993, two 30-day extreme precipitation events occur in the GL region and one in the PL region, with all events coinciding with the timing of peak of the flooding (not shown). This timing further supports the notion that both the 14 and 30-day

extreme precipitation events were significant contributors to the significant flooding that occurred in 1994. The above average precipitation seen in 2007 for the PL region is not represented by the 30-day events as compared to the 14-day events, as only one 30-day event occurs in the PL region in 2007. The smaller event count suggests the precipitous years in the PL region could be driven more so by smaller temporal scale events (i.e., 14 days) than longer scale events (i.e., 30 days).

Fig. 3.8c presents the distributions of precipitation during 30-day extreme precipitation events. First, the distribution for the WC region has a clear bi-modal structure (Fig. 3.8c, green line). There appears to be a ∼10 day period of particularly heavy precipitation, followed by a ∼10 day period of relatively low area average precipitation, and a final ∼10 day period of heavier precipitation. While the exact cause for this pattern is unknown, we can speculate it represents periodic transitions in the synoptic pattern for the WC region, commonplace in most identified events in the region. The SE and NE regions also have pronounced variability in their distribution (Fig. 3.8c, blue line and red lines respectively), though not as pronounced as the WC distribution. The event-to-event coefficient of variation for 30-day extreme precipitation events (Fig. 3.8d) differ from that for 14-day events (Fig. 3.1d). First, the average coefficient of variation across all regions is greater for 30-day events, suggesting increased event-to-event variability for 30-day events. Furthermore, the NE region has the greatest variability of the regions for 30-day events (Fig. 3.8d), while the SE region leads for 14-day events (Fig. 3.1d). These differences may indicate that certain characteristics of S2S extreme precipitation events vary regionally and with temporal scale.

3.2.2 Synoptic Composites

Fig. 3.9 presents the standardized anomalies for 500 hPa geopotential heights over the entire 30-day period. The composites again feature trough-ridge patterns specific

to each region. The NE region (Fig. 3.9a) features troughing (i.e., negative height anomalies) over the Great Lakes and the Central U.S. The ridge (i.e., positive height anomalies) is more meridionally oriented than in the 14-day events (Fig. 3.2a). This may result from greater dominance of the trough in 30-day events than in the 14-day events (Fig. 3.6e). For the SE region, greater negative height anomalies, relative to the magnitude of the corresponding positive anomalies, exist (Fig. 3.9b). These greater negative anomalies also suggests troughing to the west of the region is an important feature for 30-day extreme precipitation events. The GL and PL regions (Fig. 3.9c and d, respectively) have very similar trough-ridge patterns for 14-day and 30-day extreme precipitation (compare Figs. 3.2c and 3.2d with Figs. 3.9c and 3.9d, respectively). The area of maximum ridging for the MW region is shifted west for 30-day events (Fig. 3.9e) from its location in 14-day events (Fig. 3.2e). Finally, the WC region height composite features the same meridional dipole in the Eastern Pacific for both 30-day (Fig. 3.9f) and 14-day events (Fig. 3.2f). However, the ridging signal in Southeast Canada is more prominent in the 30-day composites. This ridging signal actually increases in magnitude as WC 14-day extreme precipitation events progress (not shown). Thus, composites of longer duration events (i.e. 30 days) would likely capture this downstream ridge.

Investigation of 200 hPa zonal winds for 30-day extreme precipitation events (Fig. 3.10) yield similar features to the corresponding 14-day composites (Fig. 3.3). All regions have at least one area of positive zonal wind anomalies, signaling an amplified jet stream. A notable difference between the 30-day and 14-day composites is the magnitude of the anomalies, yet statistically significant anomalies still exist for the 30-day composite anomalies. Most regions fall in the left-exit region of positive u-wind anomalies, supporting upper level divergence and synoptic scale lift (Bluestein, 1993). The GL and WC regions are exceptions, where broad zonal areas of positive anomalies are co-located with the regions themselves. While upper level divergence is likely a

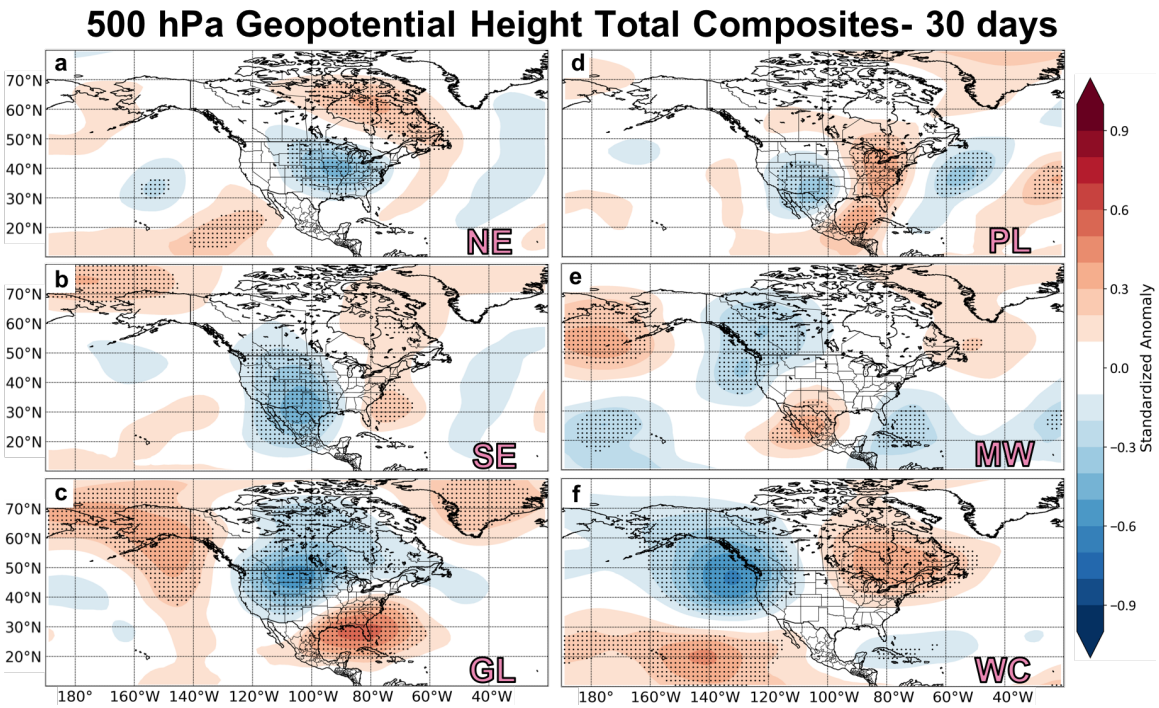

Figure 3.9: As in Fig. 3.2, but for 30-day extreme precipitation events.

key contributor to forcing a synoptic pattern favorable for extreme precipitation in these regions, variability between events may lead to an ill-defined location of the jet (Figs. 3.10c and f). The PL region has the greatest shift in zonal wind anomaly maxima between the 30-day (Fig. 3.10d) and 14-day (Fig. 3.3d) composites: the 30-day composites show amplified zonal winds centered over Texas versus Northwest Mexico in 14-day composites.

As for IVT composites for 30-day extreme precipitation events, each region features enhanced vapor transport in Fig. 3.11. As in the previous 30-day composite figures (Figs. 3.9 and 3.10), the magnitudes of the standardized anomalies are reduced in the 30-day composites compared to the 14-day composites (Fig. 3.4). Yet, the patterns of IVT anomalies are relatively similar, with cyclonic and anticyclonic IVT features visible across multiple regions. Every region has water vapor transport from the either the Pacific, Atlantic, and/or Gulf of Mexico. Similar to the 14-day

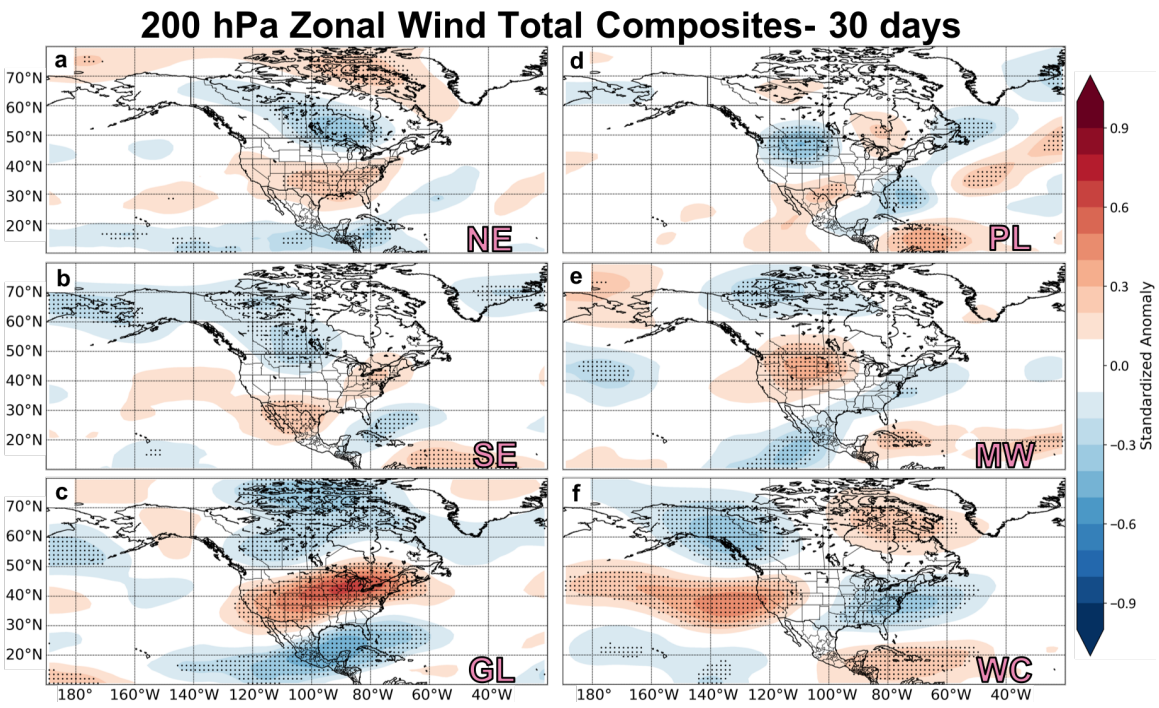

Figure 3.10: As in Fig. 3.3, but for 30-day extreme precipitation events.

IVT composites (Fig. 3.4c and e), the SE and PL regions have anomalous westerly flow in the east Pacific in Fig. 3.11c and e. This Pacific moisture feed appears more pronounced in the 30-day composites. Overall, IVT anomalies suggest moisture transport is also an important feature in 30-day extreme precipitation events.

Fig. 3.12 displays the difference in IVT between the lower and upper troposphere for 30-day extreme precipitation events. Again, the regions with the Gulf of Mexico as a moisture source (i.e. SE, GL, PL, and MW regions) have lower-level dominant IVT into that region. The greatest difference between Figs. 3.5 and 3.12 is the reduced influence of the upper-level IVT in 30-day extreme precipitation events. The SE and WC regions (Fig. 3.12c and f, respectively) have reduced influence from upper level moisture transport, where as in Fig. 3.5c and f, respectively, upper level IVT has a larger influence in particular areas. This difference could be a result of the weaker 30-day event 200 hPa zonal wind anomalies (Fig. 3.10), a change in the fundamental

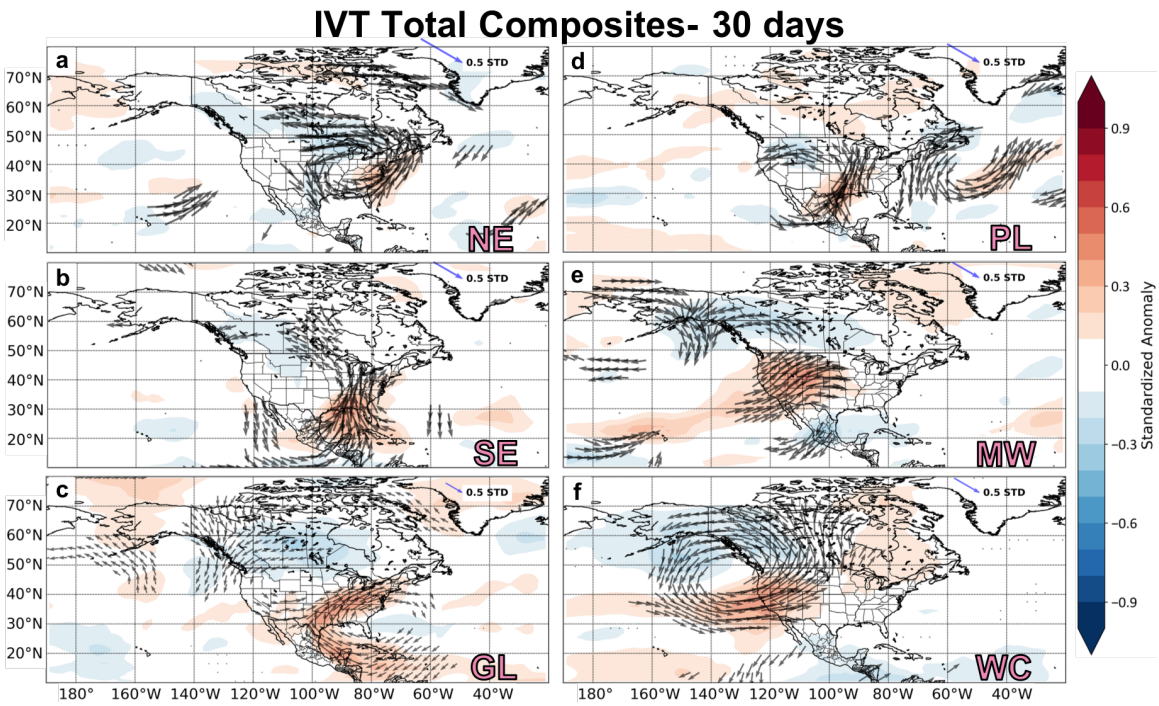

Figure 3.11: As in Fig. 3.4, but for 30-day extreme precipitation events.

characteristics of IVT for a longer period (i.e. 30 days) extreme precipitation event, or averaging over 30 days instead of 14.

3.2.3 Atmospheric Rivers

To investigate any connections between 30-day extreme precipitation events and ARs, we again use the Guan and Waliser (2015) AR database to calculate regional AR days (i.e. landfalling AR activity). Fig. 3.13a displays the AR day frequency for 30-day extreme event days and non-extreme event days. All regions have increased frequency of AR days during 30-day events compared to non-event days, with the WC, MW, and GL regions having the greatest increase. These regions have the strongest connection between increased AR activity and 30-day extreme precipitation events. Compared to Fig. 3.7a, the percentage of AR days during events is reduced in all regions, especially in the SE and GL regions. This is an expected result as the 14-day events likely have more frequent occurrence of heavy precipitation days (compare

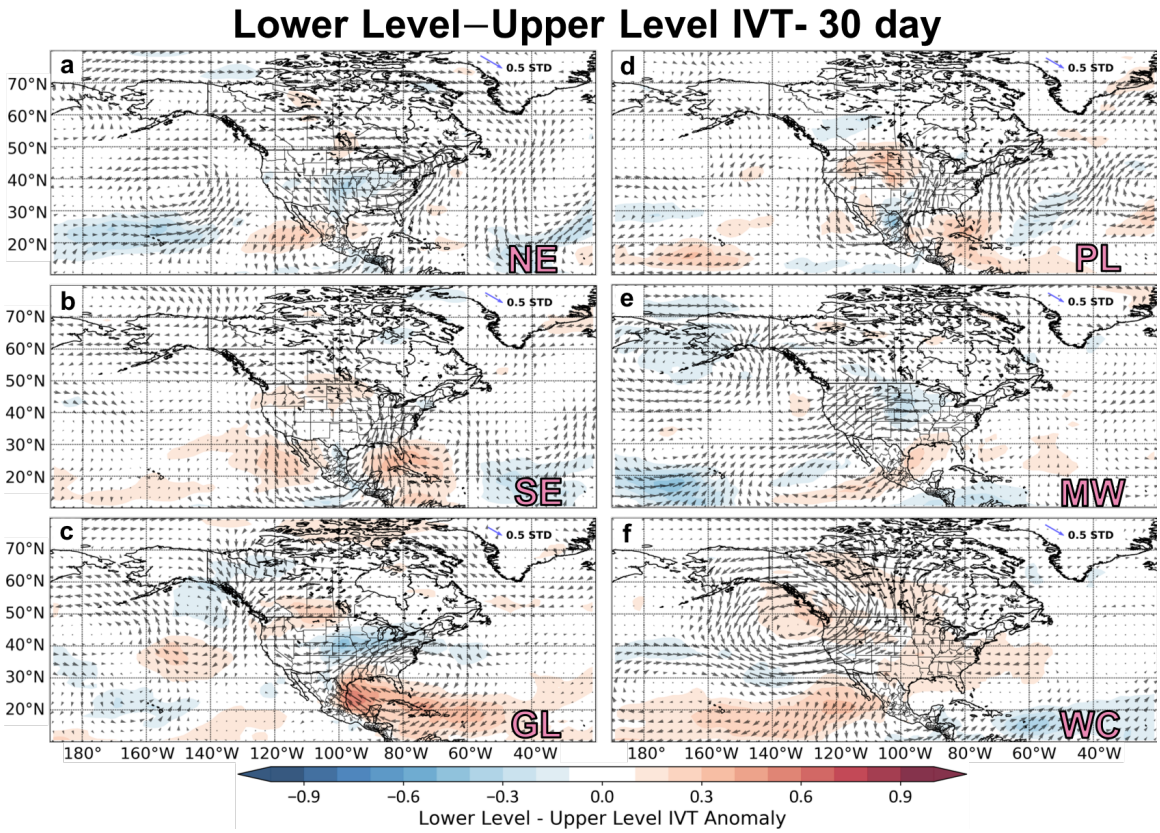

Figure 3.12: As in Fig. 3.5, but for 30-day extreme precipitation events.

Figs. 3.1c and 3.8c) and AR contributions compared to 30-day events. The MW region (Fig. 3.13a) only has a slight decrease in AR day frequency for 30-day event days from the 14-day event days (Fig. 3.7a), thus ARs may be a more important characteristic of 30-day extreme precipitation events than 14-day events in the MW region, in respect to other regions.

We consider the number of 30-day extreme precipitation events meeting or exceeding the significant number of AR days for a 30-day period in Fig. 3.13b. If an event meets or exceeds this threshold, it represents an anomalous increase in ARs days in that specific 30-day period. The MW and WC regions stand out with the greatest percentage of 30-day events with a significant increase in AR days, suggesting AR activity is particularly important in these regions. Contrarily, only one 30-day event in the PL region has a significant increase in AR days. The percentages in Fig. 3.13b

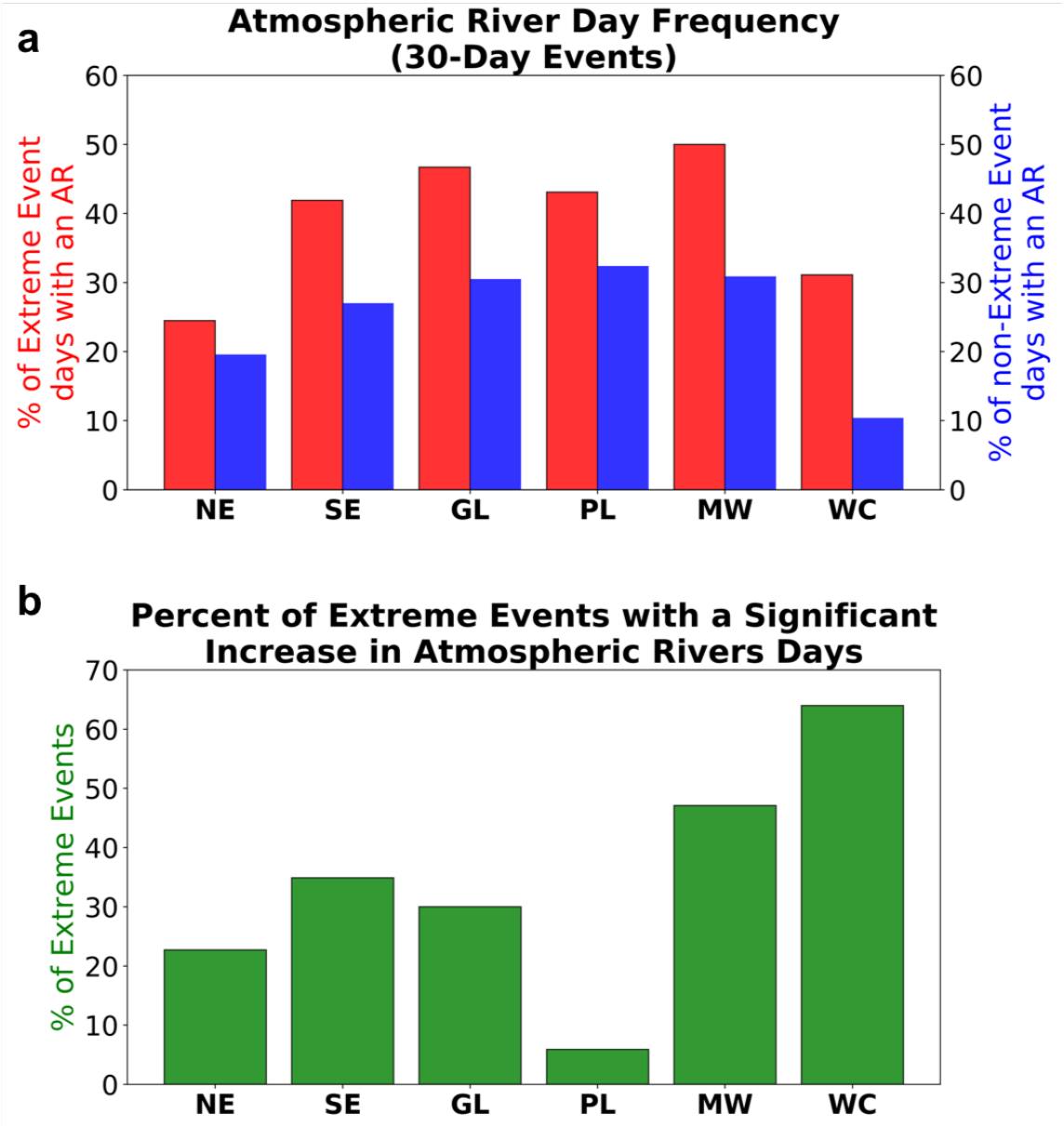

Figure 3.13: As in Fig. 3.7, but for 30-day extreme precipitation events.

are less then those for 14-day events in Fig. 3.7b, except for the MW and WC regions, which is consistent with the changes between Figs. 3.7a and 3.13a, where we see the least percent change to the percent of AR days during events for the MW and WC regions. The analysis in Fig. 3.13b indicates AR activity significantly increases in some 30-day events, particularly in the MW and WC regions.

Chapter 4

Precursors to 14-day Extreme Precipitation Events

Thus far, we have examined fundamental atmospheric characteristics that occur *during* the event. As Figs. 3.6a-d indicate, however, some regions have synoptic patterns in place *before* events begin. In this chapter, we analyze lag composites of synoptic variables to reveal whether there are significant atmospheric precursors to 14-day events, which could improve the skill of forecasting these events. We also examine several modes of climate variability for their utility in the prediction of 14-day extreme precipitation events. 14-day events are chosen over 30-day events for this analysis as the shorter temporal scale of 14-day events may capture more discernible patterns, but similar analysis can be performed on 30-day events and is left for future research.

4.1 Synoptic Lag Composites

Figure 4.1 displays both the Day -10 to -6 and Day -5 to -1 (Day -1 represents the day before the start of the 14-day extreme precipitation event) averaged 500 hPa geopotential height standardized anomalies for each of the six regions. In the Day -5 to -1 window, several regions feature similar patterns to their corresponding total event composites (Fig. 3.2). All regions except the WC region have similar trough and ridge anomalies to their event composites, but with anomalies shifted upstream to the west and northwest of the locations seen in Fig. 3.2. The NE region (Fig. 4.1a) features the developing trough in the western Great Lakes but lacks the downstream ridge noted in Figs. 3.6a and b. The WC and MW regions (Figs. 4.1i and k) both have meridional dipoles in the form of an Alaskan ridge and North Pacific trough.

Ridging over Alaska and in the Gulf of Alaska is a common feature in several regions, but particularly in GL region during the Day -5 to -1 window (Fig. 4.1e).

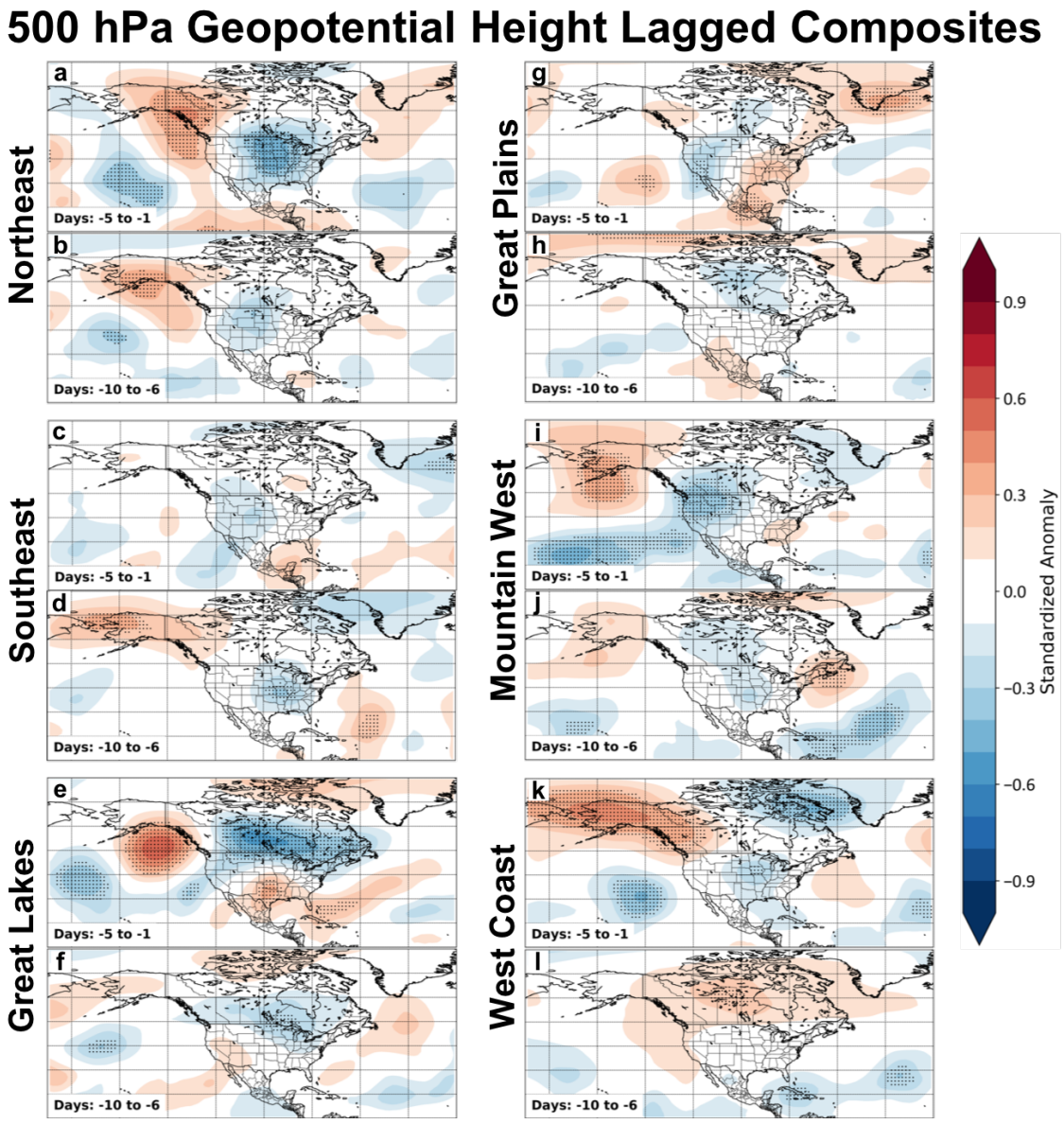

Figure 4.1: Composite of 500 hPa geopotential height standardized anomalies for lagged windows of -10 to -6 and -5 to -1 days (before the first day of an extreme event). Statistically significant anomalies ($p < 0.05$) are stippled.

Looking further back to Days -10 to -6 (Figs. 4.1b,d,f,h,j and l), the CONUS itself is void of any statistically significant geopotential height anomalies. Again, the

Alaskan ridge signal emerges as a significant precursor for 14-day extreme precipitation events in the NE, SE, and MW regions (Figs. 4.1b,d,j). The reversal in polarity of the height dipole in the WC region identified in Fig. 3.6c and d is depicted in the Day -10 to -6 composite as well, albeit much weaker in magnitude. Increased event-to-event variability in synoptic flow likely contributes to some to the weakening in the strength of the signals in this window.

The same lag composite analysis is performed on 200 hPa zonal wind in Fig. 4.2. Days -5 to -1 composite-mean zonal wind patterns correspond less with the event total composite patterns (Fig. 3.3) than the geopotential height composites. The GL and MW regions (Figs. 4.2e and i) are the only two which resemble the total event composites (Figs. 3.3c and e), though the GL region is the only region of the two with statistically significant anomalies (Fig. 4.2e). In the GL region, an amplified jet is located over the north-central U.S. and Alaska, suggesting an active synoptic weather pattern. This notion is supported by the Day -5 to -1 geopotential height anomaly composites for the GL region (Fig. 4.1e). Additionally, the MW and WC regions (Figs. 4.2i and k) both feature anomalously weak zonal winds near or south of the Gulf of Alaska. The weaker zonal winds, along with their respective geopotential height composites (Figs. 4.1i and k), suggest a developing Alaskan ridge before 14-day extreme precipitation events begin for the two westernmost CONUS regions.

As in Fig. 4.1, the Day -10 to -6 composites (Figs. 4.2b,d,f,h,j, and l) have weak zonal wind anomalies, likely due to increased variability in synoptic flow. The GL region (Fig. 4.1f) features the only significant anomaly over the CONUS, which is similar to the amplified jet in the Day -5 to -1 composite (Fig. 4.2e) but with reduced magnitude. Several regions (e.g. NE, SE, GL, and MW) feature weak zonal wind anomalies in the North Pacific in their Day -10 to -6 composite means (Fig. 4.2b,d,f, and j), suggesting patterns conducive to CONUS 14-day extreme precipitation events may develop upstream several days before events begin in some cases.

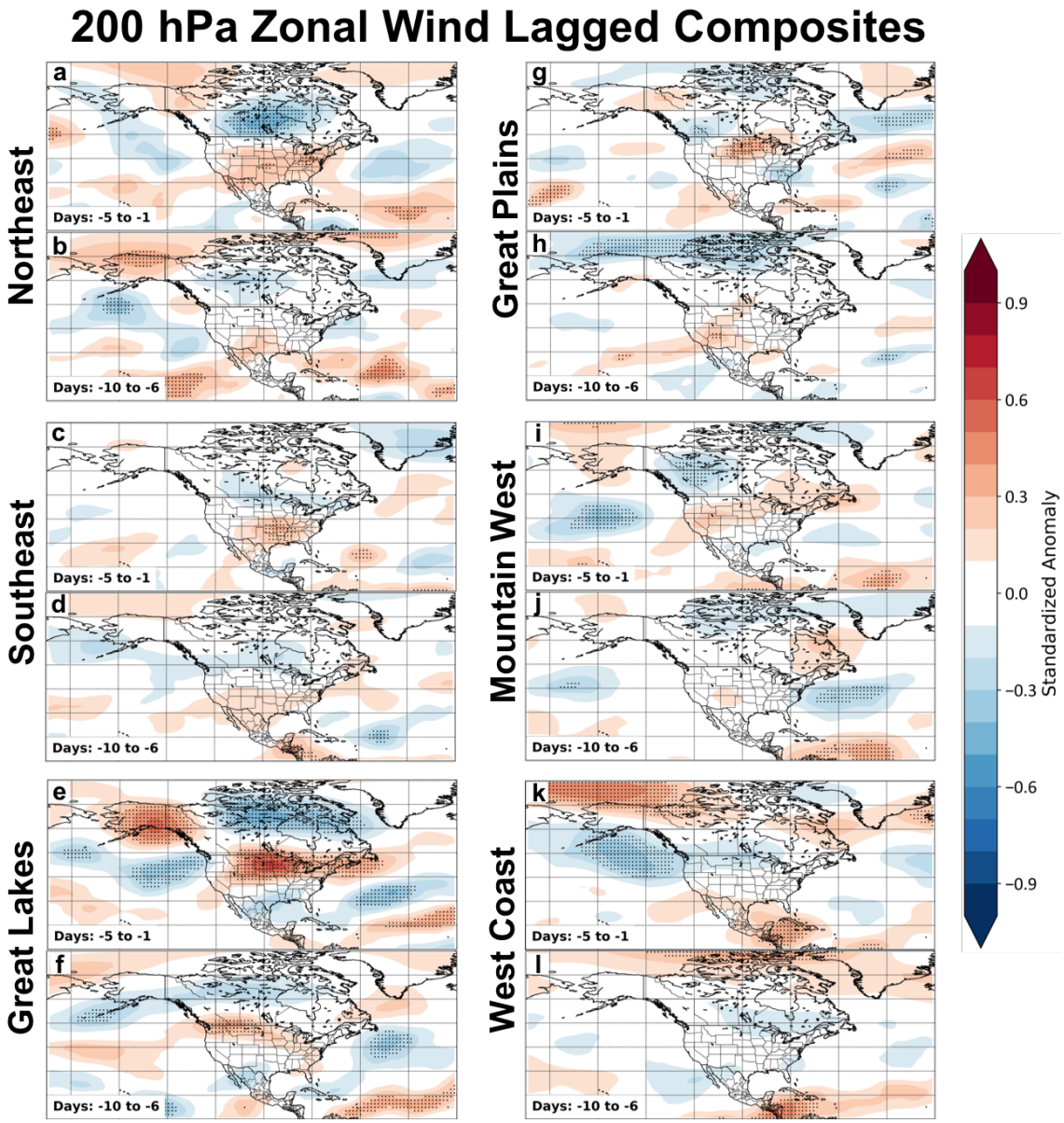

Figure 4.2: As in Fig. 4.1, but for 200 hPa zonal winds.

4.2 Modes of Climate Variability

To examine the utility of large-scale climate modes in forecasting 14-day extreme precipitation events across the CONUS, we conduct lag composite analysis on the standardized indexes of four key climate modes for US weather variability: the AO, the NAO, the PNA, and the NPO (Fig. 4.3). While never reaching a level of significance, AO signal appears in the NE and GL regions (Figs.4.3a and c), with a positive AO 12 to 5 days before 14-day extreme precipitation events begin in the NE region turning slightly negative during the event. In the GL region, the AO is positive about a week before events and continues in that polarity until the final days of the event. Interestingly, the normally closely-related NAO is out of phase with the AO in the GL region, particularly near the start of the 14-day extreme precipitation events, where it becomes significantly negative. Anomalously high heights over the North Atlantic and troughing over Eastern North America, a blocking pattern commonly associated with a negative NAO, would suggest increased precipitation in the GL region, but is not clearly identified in Fig. 3.2c. The opposing signs of the NAO and AO suggests a more active synoptic pattern is in place over North America, possibility with more shortwave activity, while a more zonal flow is in place over the Northern Hemisphere as a whole. The region with the strongest and most significant NAO signal is the PL region (Fig. 4.3d), where a negative composite mean index value occurs near the start of 14-day extreme precipitation events. This significant negative NAO signal again suggests downstream blocking occurs towards the beginning of events. Both the MW and WC regions (Figs. 4.3e and f) have a generally positive NAO. Although far from the North Atlantic, downstream blocking may support slowed synoptic wave propagation upstream, keeping these regions in a troughing dominated regime.

The PNA possesses detectable signals for several regions. A positive PNA (characterized by troughing in the North Pacific, ridging in Western North America, and troughing in Eastern U.S.) pattern exists during events in the NE region (Fig.4.3a)

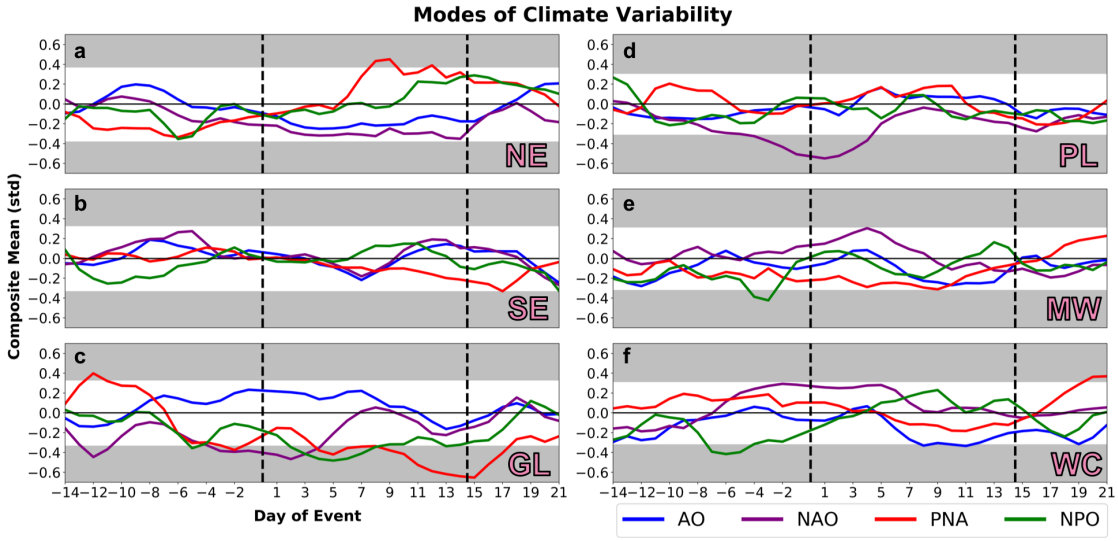

Figure 4.3: Lag composite timeseries for the AO (blue), NAO (purple), PNA (red), and NPO (green) (standardized) before, during, and after 14-day extreme precipitation events as a function of region. The level for significance ($p < 0.05$) is denoted by gray background shading, as determined by the most robust level of the four timeseries.

and precedes events in the GL, PL, and WC regions (Figs.4.3c,d,f). The significant positive PNA signature makes sense for the NE region given the characteristic troughing patterns in its corresponding height composite (Fig. 3.2a). The height anomaly patterns for the GL region (Fig. 3.2c) during 14-day extreme precipitation events match remarkably well with the PNA pattern. Indeed, the notion that the ridge-trough-ridge pattern in the GL region closely resembles the characteristic negative PNA pattern is supported by the negative PNA signal in Fig.4.3c. The last mode of climate variability considered is the NPO, which has the greatest connection to 14-day extreme precipitation events in the GL and WC regions (Figs. 4.3c and f). A negative NPO signal is apparent throughout the 14-day event period in the GL region and significantly negative for several days during events, likely a link to the anomalously high geopotential heights in the North Pacific (Fig. 3.2c). In the WC region, the NPO shifts from negative to positive near the start of events. The North Pacific 500 hPa height pattern for the WC region composite features a meridional dipole pattern like

that of the positive phase of the NPO, albeit displaced to the southeast (Fig. 3.2f). As previously discussed, there is a reversal in the height patterns for the WC regions (Figs. 3.6c and d). This change in height anomalies is mirrors the flip from negative NPO to positive NPO (Fig. 4.3f). While not applicable in every event, these modes of climate variability may have some connection to 14-day extreme precipitation events due to their corresponding synoptic anomaly patterns.

Finally, we consider the ties between the MJO and our 14-day extreme precipitation events. This teleconnection pattern may influence North American precipitation through Rossby wave prorogation into the mid-latitudes causing changes to storm tracks and precipitation anomalies (e.g., Zheng et al., 2018). The link between the MJO and subsesaonal precipitation across North America may help to improve the prediction of extreme precipitation (Jones et al., 2004; Jones and Carvalho, 2012). Figure 4.4 presents heat maps of MJO phase lag composites for Days -10 to -6 (Fig. 4.4a), Days -5 to -1 (Fig. 4.4b), and Days +1 to +5 (Fig. 4.4c). Although several MJO phases are statistically significant for different regions, one major finding is that there is an absence of a true 'evolution' of the MJO; i.e., where the MJO advances sequentially in phase with time. Other conclusions about MJO phases also arise. First, MJO phases 6 and 7 (5 and 6) are more common over all regions during Days -10 to -6 (-5 to -1) versus than other phases. Phases 1 through 3 are the less common MJO phases preceding 14-day extreme precipitation events. During the first five days of the event, phases 1, 5, and 6 are more common than 3, 4 and 8.

Working from a regional framework, the WC region has the most common MJO phase progression from phase 4 to phase 5 to no significant phase during events (Fig. 4.4). Mundhenk et al. (2018) suggests a connection between increased AR activity in California in the few days after an MJO phase 7 event. This analysis neither confirms or rebuts this, as the frequency of MJO phase 7 events is insignificant for the WC region for all lags. However, for the WC region, MJO phase 7 is more common before

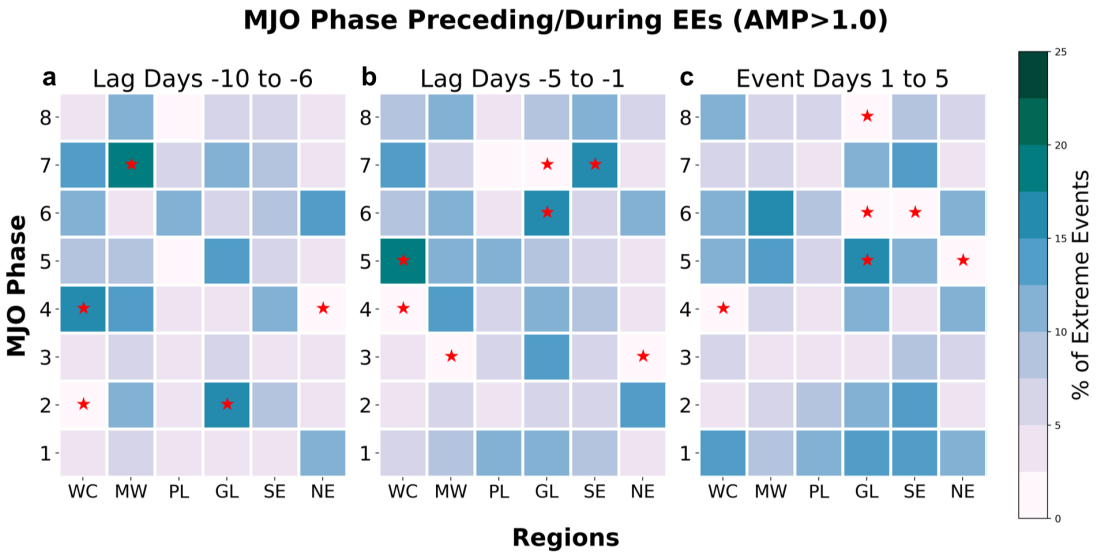

Figure 4.4: Heatmap of MJO phase occurrence in each region for lag windows of -10 to -6 days, -5 to -1 days, and the first 5 days of the event. The daily MJO phase is based on the Wheeler and Hendon (2004) Real-time Multivariate MJO series 1 (RMM1) and 2 (RMM2). To determine the MJO phase during the five day windows, the mode is chosen as the window phase if it occurs in at least three of the five days. Only windows with an average five day amplitude of $\geq$1.0 are considered. Red stars indicate the composite percentages of occurrence for MJO phases before/during 14-day extreme precipitation events are significantly different than the mean percentage of occurrence of particular phases (roughly 7-8%). This significance test is based on a two-tailed bootstrapping test (p-value of 0.05), with 5,000 iterations and assists in identifying, common and uncommon phases of the MJO before and during events.

events than during events. Meanwhile, MJO phase 7 is significantly more common in the MW region during the -10 to -6 day lag window. The GL region has aspects of some progression between phase 2 to phase 5 from the Days -10 to -6 lag to Days +1 to +5. Outside of these two regions, there are no identifiable patterns of MJO phase propagation. The features identified in Fig. 4.4 may have some use in aiding prediction of extreme precipitation, but the complex nature of these 14-day extreme precipitation events prohibit a stronger correlation.

Chapter 5

Summary and Discussion

In summary, S2S extreme precipitation can lead to great societal impacts, leading to a need for greater understanding and prediction. While many studies have focused on daily extremes and individual synoptic systems, investigation into events on the S2S timeframe is lacking. Analyzing large-scale 14-day and 30-day extreme precipitation events based on the 95^{th} percentile of precipitation, among other considerations, is a suitable place to begin exploration into S2S precipitation extremes. Working with specific pre-defined regions within the CONUS allows for more accurate representations of regional drivers of these events.

14-day extreme precipitation events vary seasonally, similarly to each region's annual precipitation cycle (Fig. 3.1a). General synoptic patterns which characterize a 14-day extreme precipitation event include a 500 hPa trough/ridge dipole with the trough axis positioned to the west of the region of interest (Fig. 3.2). The location of the greatest positive height anomaly in respect to the event area varies by region. Troughing is found to be more frequent than ridging in the NE and WC regions from Fig. 3.6. This troughing dominance is apparent in all regions outside of the GL region, where a Southeast U.S. ridge may be a more perpetual feature. Furthermore, an anomalous increase in 200 hPa zonal winds and IVT into each region provides a favorable set-up for synoptic scale precipitation, as shown in Fig. 3.3 and 3.4, respectively. Additionally, Fig. 3.5 identifies favorable set-ups for the direction and level (upper or lower) of IVT in each region. Finally, there is a significant uptick in the AR frequency for each region, with the SE, GL, and WC regions having the greatest increase (Fig. 3.7). These synoptic characteristics are similar across the CONUS, except the exact set-up varies from region to region.

30-day extreme precipitation events share many similarities to 14-day events in both event and synoptic characteristics. A major contributor to the similarities is fact that many 30-day events overlap with 14-day events. As for 14-day events, the seasonal frequency is similar to annual precipitation cycles in 30-day events (Fig. 3.8a). A key difference between the two set of events is the coefficient of variation. 30-day events (Fig. 3.8d) have a much larger coefficient of variation than 14-day events (Fig. 3.1d), suggesting greater event-to-event variability in precipitation totals in 30-day events. Additionally, the NE region has the greatest coefficient of variation for 30-day events, where as the SE region takes the top spot in 14-day events.

For the composites of synoptic variables, 30-day events (Figs. 3.9-3.12) featured similar patterns to the 14-day events (Figs. 3.2-3.5), albeit with decreased magnitudes in anomalies. As for the 14-day events, 500 hPa geopotential height anomalies feature troughing signals positioned west of the region and a ridge with regionally varying spacial relation to the trough (Fig. 3.9). The location of the ridge in the NE, MW, and WC regions differ the greatest in Fig. 3.9a,e,f (respectively) from their 14-day composites in Fig. 3.2a,e,f. Likewise, the zonal wind anomalies in Fig. 3.10 are very similar to those in Fig. 3.3, suggesting an enhanced zonal jet is a significant feature in for 30-day extreme precipitation events. Although the magnitudes of IVT anomalies are not as large in Fig. 3.11 (30-day events) compared to Fig. 3.4 (14-day events), significant, large-scale increases to moisture transport from the Atlantic, Gulf of Mexico, the Pacific, or some combination of the three is a necessary feature for extreme precipitation for each region and for both event sets. Further, the importance of upper-level IVT and lower-level IVT varies in the GL and PL regions (Fig. 3.12c and d, respectively). This difference may help in distinguishing sources of moisture and would be useful for forecasting applications. There is a significant up-tick in the AR frequency for each region, with the MW and WC regions having the greatest increase during 30-day extreme precipitation events (Fig. 3.13).

Attempting to identify precursor features of these events has proved difficult, as analysis of synoptic lagged patterns and modes of climate variability for 14-day extreme precipitation events produced mixed results. Identifiable features in 500 hPa geopotential height (Fig. 4.1) and 200 hPa zonal wind (Fig. 4.2) composite anomalies were apparent in many regions in the Day -5 to -1 lag window including ridging and zonal wind anomalies in the North Pacific. In the Day -10 to -6 day window, statistically significant anomalies are confined to the North Pacific where varying jet and height patterns occur (Figs. 4.1/4.2b,d, and f). In an attempt to improve upon these lead time features, modes of variability including the NPO, AO, NAO, PNA, and the MJO are considered. A few regions have detectable signals in these indices. A positive PNA in the GL region, a negative NAO in the PL region, and a trend toward more a more positive NPO in the WC region are some of the stronger signals. For the MJO, phases 5-7 have the greatest occurrence in the event days 1 to 5 in Fig. 4.4c, but our findings lack a true sequential progression of MJO phase. Unfortunately, the composites of these modes do not diagnose clear precursors for our 14-day extreme precipitation events.

Many aspects of these results agree with previous literature on extreme precipitation. The location of the troughing with relation to precipitation area is similar to 500 hPa cyclone centers in Konrad (2001) analysis of 2-day extreme precipitation events. The anomalously high heights to the northeast of the NE region is more of a downstream ridge compared to other regions (Fig. 3.2a), possibly suggesting that this ridge could be amplified by advecting diabatic heat released from the condensating precipitation over the NE (e.g. Aubert, 1957). This is one possible explanation for the lagging precursor signal in the ridge index (Fig. 3.6b). Furthermore, the upstream ridge signal disappears quickly after the event has ended, again suggesting a close association with NE region precipitation.

Additionally, Konrad (2001) suggests other aspects of the synoptic environment, beyond 500 hPa troughing, are necessary for extreme precipitation, such as moisture advection and wind direction. In addition to geopotential height anomalies, our study identifies some of these additional aspects including enhanced IVT, strong upper-level zonal winds, and increased AR frequency. Although their precipitation regions were determined by hierarchical clusters, the orientation of the trough ridge dipoles in Zhao et al. (2017), along with the cyclonic and anticyclonic IVT anomalies, fit patterns seen in this analysis (i.e., Figs. 3.2 and 3.9). The percentage of ARs days during extreme precipitation events in the SE are similar to work done by Mahoney et al. (2016), which found between 40-60% (varying seasonally and spatially) of daily events in the Southeast U.S. were associated with a an AR. Likewise, the near 60% (45%) of 14-day (30-day) event days corresponding with ARs in the GL region (Figs. 3.7 and 3.13), supports the 60-70% AR connection to annual maxima floods in a similar region (e.g., Lavers and Villarini, 2013). Due to the lack of more statistically significant results in the analysis of modes of climate variability conducted here, it is difficult to connect those results with previous literature.

This work represents a first-look at S2S extreme precipitation events and, as such, contains several caveats which should be addressed. Although many regions have seasonality in event distributions, the lack of seasonal considerations in this work may lead to less anomalous indices of modes of climate variability. Touma et al. (2018) concluded that different CONUS regions have differing scales of precipitation, depending on the season, and Zhao et al. (2017) identified differences in the magnitude of synoptic patterns between the warm and cold season in the CONUS. Furthermore, seasonal considerations for modes of climate variability would help connect modes to their seasonal patterns of geopotential height and precipitation anomalies. For example, considering only cool-season events, when the NAO is most active, could offer additional connections. The regions themselves may also play a role into some

variability in results. While the regions chosen for our study are expansive enough to capture large scale events, precipitation characteristics may not be the same throughout a specific region. For example, Flanagan et al. (2018) identified different features in the Northern Great Plains as compared to the Southern Great Plains for pluvial years. The patterns identified in this study ignore the differences between these two areas, yet are similar in scale and orientation to the ones found in Flanagan et al. (2018). Furthermore, a strict boarder for each region does not allow for events that occur between regions to be identified.

Observed in the PL region, magnitudes for synoptic features in 14-day events in Figs. 3.2d-3.4d are less than in other regions. This difference in magnitude may be attributed to differences in precipitation characteristics, such as precipitation drivers/scale. For instance, Great Plains extreme precipitation has been shown to be more driven by mesoscale convective systems (MCSs) than synoptic forcing (Schumacher and Johnson, 2006), with parts of the region receiving over 60% of their May-August rainfall from MCSs (Haberlie and Ashley, 2019). This would account for weaker synoptic anomalies in the PL and further supported by the fact that PL events peak in the warm season, when MCSs are more common. Interestingly, composite anomalies for 30-day events in the PL region did not share this relatively diminished magnitude in Figs. 3.9d-3.11d. This may be a result of the reduction in magnitudes seen overall in 30-day composites compared to the 14-day composites, hypothesized to be a product of decreased frequency of precipitous days in the 30-day event period and compositing a larger number of days.

Going forward, there is still much to be learned about S2S extreme precipitation events. For example, it is still unknown what exact drivers of precipitation are the most favorable features (i.e., MCS, tropical, synoptic isotropic ascent, etc.) for each region. Further, additional investigation into precursors for extreme precipitation and the utility of numerical, statistical, and climate models would aid in the prediction of

events. Other possible precursors include sea surface temperatures and soil moisture anomalies. The effects of climate change change on extreme precipitation thresholds and the nature of S2S extreme precipitation events should also be a future consideration. Finally, looking beyond the constraints of a 14 or 30 day window to a windows of other or more flexible temporal scales should advance our overall understanding of S2S events.

Bibliography

Alexander, L. V., et al., 2006: Global observed changes in daily climate extremes of temperature and precipitation. *Journal of Geophysical Research Atmospheres*, **111**, doi:10.1029/2005JD006290.

Armal, S., N. Devineni, and R. Khanbilvardi, 2018: Trends in extreme rainfall frequency in the contiguous United States: Attribution to climate change and climate variability modes. *Journal of Climate*, **31 (1)**, 369–385, doi:10.1175/JCLI-D-17-0106.1.

Aubert, E. J., 1957: On the release of latent heat as a factor in large scale atmospheric motions. *Journal of Meteorology*, **14 (6)**, 527–542, doi:10.1175/1520-0469(1957)014⟨0527:OTROLH⟩2.0.CO;2.

Batté, L., C. Ardilouze, and M. Déqué, 2018: Forecasting West African heat waves at subseasonal and seasonal time scales. *Monthly Weather Review*, **146 (3)**, 889–907, doi:10.1175/MWR-D-17-0211.1.

Baxter, S. and S. Nigam, 2015: Key role of the North Pacific Oscillation-West Pacific pattern in generating the extreme 2013/14 North American Winter. *Journal of Climate*, **28 (20)**, 8109–8117, doi:10.1175/JCLI-D-14-00726.1.

Bluestein, H. B., 1992: *Synoptic-Dynamic Meteorology in Midlatitudes*, Vol. 1. Oxford University Press, 338-343 pp.

Bluestein, H. B., 1993: *Synoptic-Dynamic Meteorology in Midlatitudes*, Vol. 2. Oxford University Press, 397-399 pp.

Brunet, G., et al., 2010: Collaboration of the weather and climate communities to advance subseasonal-to-seasonal prediction. *Bulletin of the American Meteorological Society*, **91 (10)**, 1397–1406, doi:10.1175/2010BAMS3013.1.

Chiodi, A. M., N. A. Bond, N. K. Larkin, and R. J. Barbour, 2016: Summertime rainfall events in Eastern Washington and Oregon. *Weather and Forecasting*, **31 (5)**, 1465–1480, doi:10.1175/waf-d-16-0024.1.

Collow, A. B. M., M. G. Bosilovich, and R. D. Koster, 2016: Large-scale influences on summertime extreme precipitation in the Northeastern United States. *Journal of Hydrometeorology*, **17 (12)**, 3045–3061, doi:10.1175/jhm-d-16-0091.1.

Daly, C., G. H. Taylor, W. P. Gibson, T. W. Parzybok, G. L. Johnson, and P. A. Pasteris, 2000: High-quality spatial climate data sets for the United States and beyond. *Transactions of the ASAE*, **43 (6)**, 1957–1962, doi:10.13031/2013.3101.

Dee, D. P., et al., 2011: The ERA-Interim reanalysis: configuration and performance of the data assimilation system. *Quarterly Journal of the Royal Meteorological Society*, **137 (656)**, 553–597, doi:10.1002/qj.828.

Dettinger, M. D., F. M. Ralph, and J. J. Rutz, 2018: Empirical return periods of the most intense vapor transports during historical atmospheric river landfalls on the U.S. West Coast. *Journal of Hydrometeorology*, **19 (8)**, 1363–1377, doi:10.1175/jhm-d-17-0247.1.

Dong, L., L. R. Leung, F. Song, and J. Lu, 2018: Roles of SST versus internal atmospheric variability in winter extreme precipitation variability along the U.S. West Coast. *Journal of Climate*, **31 (19)**, 8039–8058, doi:10.1175/JCLI-D-18-0062.1.

Flanagan, P. X., J. B. Basara, J. C. Furtado, and X. Xiao, 2018: Primary atmospheric drivers of pluvial years in the United States Great Plains. *Journal of Hydrometeorology*, **19 (4)**, 643–658, doi:10.1175/jhm-d-17-0148.1.

Frei, A., K. E. Kunkel, and A. Matonse, 2015: The seasonal nature of extreme hydrological events in the Northeastern United States. *Journal of Hydrometeorology*, **16 (5)**, 2065–2085, doi:10.1175/jhm-d-14-0237.1.

Gershunov, A., 1998: ENSO influence on intraseasonal extreme rainfall and temperature frequencies in the contiguous United States: Implications for long-range predictability. *Journal of Climate*, **11 (12)**, 3192–3203, doi:10.1175/1520-0442(1998)011⟨3192:EIOIER⟩2.0.CO;2.

Gitro, C., M. Evans, and R. Grumm, 2014: Two major heavy rain/flood events in the mid-Atlantic: June 2006 and September 2011. *Journal of Operational Meteorology*, **2**, 152–168, doi:10.15191/nwajom.2014.0213.

Guan, B. and D. E. Waliser, 2015: Detection of atmospheric rivers: Evaluation and application of an algorithm for global studies. *Journal of Geophysical Research: Atmospheres*, **120 (24)**, 12 514–12 535, doi:10.1002/2015JD024257.

Guan, B., D. E. Waliser, N. P. Molotch, E. J. Fetzer, and P. J. Neiman, 2012: Does the Madden–Julian Oscillation influence wintertime atmospheric rivers and snowpack in the Sierra Nevada? *Monthly Weather Review*, **140 (2)**, 325–342, doi:10.1175/MWR-D-11-00087.1.

Haberlie, A. M. and W. S. Ashley, 2019: A radar-based climatology of mesoscale convective systems in the United States. *Journal of Climate*, **32 (5)**, 1591–1606, doi:10.1175/JCLI-D-18-0559.1.

Hirata, F. E. and A. M. Grimm, 2017: The role of synoptic and intraseasonal anomalies on the life cycle of rainfall extremes over South America: non-summer conditions. *Climate Dynamics*, **49 (1)**, 313–326, doi:10.1007/s00382-016-3344-8.

Jiang, R., T. Y. Gan, J. Xie, and N. Wang, 2014: Spatiotemporal variability of Alberta's seasonal precipitation, their teleconnection with large-scale climate anomalies and sea surface temperature. *International Journal of Climatology*, **34 (9)**, 2899–2917, doi:10.1002/joc.3883.

Jones, C. and L. M. V. Carvalho, 2012: Spatial-intensity variations in extreme precipitation in the contiguous United States and the Madden-Julian Oscillation. *Journal of Climate*, **25 (14)**, 4898–4913, doi:10.1175/JCLI-D-11-00278.1.

Jones, C., D. E. Waliser, K. M. Lau, and W. Stern, 2004: Global occurrences of extreme precipitation and the Madden–Julian Oscillation: Observations and predictability. *Journal of Climate*, **17 (23)**, 4575–4589, doi:10.1175/3238.1.

Karl, T. R. and R. W. Knight, 1998: Secular trends of precipitation amount, frequency, and intensity in the United States. *Bulletin of the American Meteorological Society*, **79 (2)**, 231–242, doi:10.1175/1520-0477(1998)079⟨0231:STOPAF⟩2.0.CO;2.

Kenyon, J. and G. C. Hegerl, 2010: Influence of modes of climate variability on global precipitation extremes. *Journal of Climate*, **23 (23)**, 6248–6262, doi:10.1175/2010JCLI3617.1.

Konrad, C. E., 2001: The most extreme precipitation events over the Eastern United States from 1950 to 1996: Considerations of scale. *Journal of Hydrometeorology*, **2 (3)**, 309–325, doi:10.1175/1525-7541(2001)002⟨0309:tmepeo⟩2.0.co;2.

Kottek, M., J. Grieser, C. Beck, B. Rudolf, and F. Rubel, 2006: World map of the Köppen-Geiger climate classification updated. *Meteorologische Zeitschrift*, **15**, 259–263, doi:10.1127/0941-2948/2006/0130.

Kunkel, K. E., S. A. Changnon, and J. R. Angel, 1994: Climatic aspects of the 1993 Upper Mississippi River Basin Flood. *Bulletin of the American Meteorological Society*, **75 (5)**, 811–822, doi:10.1175/1520-0477.

Lackmann, G. M., 2013: The South-Central U.S. Flood of May 2010: present and future. *Journal of Climate*, **26 (13)**, 4688–4709, doi:10.1175/JCLI-D-12-00392.1, URL `https://doi.org/10.1175/JCLI-D-12-00392.1`.

Lavers, D. A. and G. Villarini, 2013: Atmospheric rivers and flooding over the central United States. *Journal of Climate*, **26 (20)**, 7829–7836, doi:10.1175/JCLI-D-13-00212.1.

Lim, Y., S.-W. Son, and D. Kim, 2018: MJO prediction skill of the subseasonal-to-seasonal prediction models. *Journal of Climate*, **31 (10)**, 4075–4094, doi:10.1175/JCLI-D-17-0545.1.

Lynch, S. L. and R. S. Schumacher, 2014: Ensemble-based analysis of the May 2010 extreme rainfall in Tennessee and Kentucky. *Monthly Weather Review*, **142 (1)**, 222–239, doi:10.1175/mwr-d-13-00020.1.

Maddox, R. A., C. F. Chappell, and L. R. Hoxit, 1979: Synoptic and meso-α scale aspects of flash flood events. *Bulletin of the American Meteorological Society*, **60 (2)**, 115–123, doi:10.1175/1520-0477-60.2.115.

Mahoney, K., et al., 2016: Understanding the role of atmospheric rivers in heavy precipitation in the Southeast United States. *Monthly Weather Review*, **144 (4)**, 1617–1632, doi:10.1175/mwr-d-15-0279.1.

Mallakpour, I. and G. Villarini, 2016: Analysis of changes in the magnitude, frequency, and seasonality of heavy precipitation over the contiguous USA. *Theoretical and Applied Climatology*, **130 (1-2)**, 345–363, doi:10.1007/s00704-016-1881-z.

Marciano, C. G. and G. M. Lackmann, 2017: The South Carolina Flood of October 2015: Moisture transport analysis and the role of Hurricane Joaquin. *Journal of Hydrometeorology*, **18 (11)**, 2973–2990, doi:10.1175/jhm-d-16-0235.1.

Molina, M. J., J. T. Allen, and V. A. Gensini, 2018: The gulf of mexico and enso influence on subseasonal and seasonal conus winter tornado variability. *Journal of Applied Meteorology and Climatology*, **57 (10)**, 2439–2463, doi:10.1175/JAMC-D-18-0046.1.

Moore, B. J., K. M. Mahoney, E. M. Sukovich, R. Cifelli, and T. M. Hamill, 2015: Climatology and environmental characteristics of extreme precipitation events in the Southeastern United States. *Monthly Weather Review*, **143 (3)**, 718–741, doi:10.1175/mwr-d-14-00065.1.

Moron, V., P. Camberlin, and A. W. Robertson, 2013: Extracting subseasonal scenarios: An alternative method to analyze seasonal predictability of regional-scale tropical rainfall. *Journal of Climate*, **26 (8)**, 2580–2600, doi:10.1175/JCLI-D-12-00357.1.

Mundhenk, B. D., E. A. Barnes, E. D. Maloney, and C. F. Baggett, 2018: Skillful empirical subseasonal prediction of landfalling atmospheric river activity using the Madden–Julian oscillation and quasi-biennial oscillation. *npj Climate and Atmospheric Science*, **1 (1)**, doi:10.1038/s41612-017-0008-2.

National Academies of Sciences, Engineering and Medicine, 2016: Next generation earth system prediction: Strategies for subseasonal to seasonal forecasts. Tech. rep., National Academies of Sciences, Engineering and Medicine, Washington, DC. doi:10.17226/21873.

National Centers for Environmental Information, 2019: U.s. billion-dollar weather and climate disasters. NOAA, URL `https://www.ncdc.noaa.gov/billions/`, URL `https://www.ncdc.noaa.gov/billions/`.

Neiman, P. J., L. J. Schick, F. M. Ralph, M. Hughes, and G. A. Wick, 2011: Flooding in Western Washington: The connection to atmospheric rivers. *Journal of Hydrometeorology*, **12 (6)**, 1337–1358, doi:10.1175/2011JHM1358.1.

Newell, R. E., N. E. Newell, Y. Zhu, and C. Scott, 1992: Tropospheric rivers?- a pilot study. *Geophysical Research Letters*, **19 (24)**, 2401–2404, doi:10.1029/92GL02916.

Oklahoma Mesonet, 2015: Historic may rains eliminate drought. Oklahoma Mesonet, URL https://www.mesonet.org/index.php/news/article/historic_may_rains_eliminate_drought, URL https://www.mesonet.org/index.php/news/article/historic_may_rains_eliminate_drought.

PRISM Climate Group, 2017: PRISM Climate Group, http://prism.oregonstate.edu, created 10 OCT 2017, http://prism.oregonstate.edu, created 10 OCT 2017.

Rivera, E. R., F. Dominguez, and C. L. Castro, 2014: Atmospheric rivers and cool season extreme precipitation events in the Verde River Basin of Arizona. *Journal of Hydrometeorology*, **15 (2)**, 813–829, doi:10.1175/jhm-d-12-0189.1.

Robertson, A. W., A. Kumar, M. Peña, and F. Vitart, 2015: Improving and promoting subseasonal to seasonal prediction. *Bulletin of the American Meteorological Society*, **96 (3)**, ES49–ES53, doi:10.1175/BAMS-D-14-00139.1.

Rogers, J. C., 1981: The North Pacific Oscillation. *Journal of Climatology*, **1 (1)**, 39–57, doi:10.1002/joc.3370010106.

Rutz, J. J., W. J. Steenburgh, and F. M. Ralph, 2015: The inland penetration of atmospheric rivers over Western North America: A Lagrangian analysis. *Monthly Weather Review*, **143 (5)**, 1924–1944, doi:10.1175/mwr-d-14-00288.1.

Saharia, M., P. E. Kirstetter, H. Vergara, J. J. Gourley, and Y. Hong, 2017: Characterization of floods in the United States. *Journal of Hydrology*, **548**, 524–535, doi:10.1016/j.jhydrol.2017.03.010.

Schiraldi, N. J. and P. E. Roundy, 2017: Seasonal-to-subseasonal model forecast performance during agricultural drought transition periods in the U.S. corn belt. *Monthly Weather Review*, **145 (9)**, 3687–3708, doi:10.1175/MWR-D-17-0026.1.

Schumacher, R. S. and R. H. Johnson, 2006: Characteristics of U.S. extreme rain events during 1999–2003. *Weather and Forecasting*, **21 (1)**, 69–85, doi:10.1175/waf900.1.

Slater, L. J., G. Villarini, and A. A. Bradley, 2016: Evaluation of the skill of North-American Multi-Model Ensemble (NMME) global climate models in predicting average and extreme precipitation and temperature over the continental USA. *Climate Dynamics*, doi:10.1007/s00382-016-3286-1.

Thompson, D. W. J. and J. M. Wallace, 2000: Annular modes in the extratropical circulation. Part I: Month-to-month variability. *Journal of Climate*, **13 (5)**, 1000–1016, doi:10.1175/1520-0442(2000)013⟨1000:AMITEC⟩2.0.CO;2.

Touma, D., A. M. Michalak, D. L. Swain, and N. S. Diffenbaugh, 2018: Characterizing the spatial scales of extreme daily precipitation in the United States. *Journal of Climate*, **31 (19)**, 8023–8037, doi:10.1175/JCLI-D-18-0019.1.

U.S. Global Change Research Program, 2018: Impacts, Risks, and Adaptation in the United States: Fourth National Climate Assessment, Volume II. Tech. rep., U.S. Global Change Research Program. doi:doi:10.7930/NCA4.2018.

Vitart, F. and A. W. Robertson, 2018: The sub-seasonal to seasonal prediction project (S2S) and the prediction of extreme events. *npj Climate and Atmospheric Science*, **1**.

Vitart, F., et al., 2017: The subseasonal to seasonal (S2S) prediction project database. *Bulletin of the American Meteorological Society*, **98 (1)**, 163–173, doi:10.1175/BAMS-D-16-0017.1.

Wallace, J. M. and D. S. Gutzler, 1981: Teleconnections in the geopotential height field during the Northern Hemisphere winter. *Monthly Weather Review*, **109 (4)**, 784–812, doi:10.1175/1520-0493(1981)109⟨0784:TITGHF⟩2.0.CO;2.

Wang, H., R. Fu, A. Kumar, and W. Li, 2010: Intensification of summer rainfall variability in the Southeastern United States during recent decades. *Journal of Hydrometeorology*, **11 (4)**, 1007–1018, doi:10.1175/2010jhm1229.1.

Wang, S.-Y. S., W.-R. Huang, H.-H. Hsu, and R. R. Gillies, 2015: Role of the strengthened El Niño teleconnection in the May 2015 floods over the southern Great Plains. *Geophysical Research Letters*, **42 (19)**, 8140–8146.

Weaver, S. J., S. Baxter, and K. Harnos, 2016: Regional changes in the interannual variability of U.S. warm season precipitation. *Journal of Climate*, **29 (14)**, 5157–5173, doi:10.1175/JCLI-D-14-00803.1.

Wheeler, M. C. and H. H. Hendon, 2004: An all-Season real-time multivariate MJO index: Development of an index for monitoring and prediction. *Monthly Weather Review*, **132 (8)**, 1917–1932, doi:10.1175/1520-0493(2004)132⟨1917:AARMMI⟩2.0.CO;2.

Wick, G. A., P. J. Neiman, and F. M. Ralph, 2013: Description and validation of an automated objective technique for identification and characterization of the integrated water vapor signature of atmospheric rivers. *IEEE Transactions on Geoscience and Remote Sensing*, **51 (4)**, 2166–2176, doi:10.1109/TGRS.2012.2211024.

Zhang, C., 2013: Madden–Julian Oscillation: Bridging weather and climate. *Bulletin of the American Meteorological Society*, **94 (12)**, 1849–1870, doi:10.1175/BAMS-D-12-00026.1.

Zhao, S., Y. Deng, and R. X. Black, 2017: A dynamical and statistical characterization of U.S. extreme precipitation events and their associated large-scale meteorological patterns. *Journal of Climate*, **30 (4)**, 1307–1326, doi:10.1175/JCLI-D-15-0910.1, URL `https://doi.org/10.1175/JCLI-D-15-0910.1`.

Zheng, C., E. Kar-Man Chang, H.-M. Kim, M. Zhang, and W. Wang, 2018: Impacts of the Madden–Julian Oscillation on storm-track activity, surface air temperature, and precipitation over North America. *Journal of Climate*, **31 (15)**, 6113–6134, doi:10.1175/JCLI-D-17-0534.1.